Important Notice

UNIVERSITY OF CALGARY

Estimation of Thomsen's anisotropy parameters from compressional and converted wave surface seismic traveltime data using NMO equations, neural networks and regridding inversion

by

Amber Camille Kelter

A THESIS

SUBMITTED TO THE FACULTY OF GRADUATE STUDIES

IN PARTIAL FULFILMENT OF THE REQUIREMENTS FOR THE

DEGREE OF MASTER OF SCIENCE

DEPARTMENT OF GEOLOGY AND GEOPHYSICS

CALGARY, ALBERTA

May, 2005

UNIVERSITY OF CALGARY

FACULTY OF GRADUATE STUDIES

The undersigned certify that they have read, and recommended to the Faculty of Graduate Studies for acceptance, a thesis entitled “Estimation of Thomsen’s anisotropy parameters from compressional and converted wave surface seismic traveltime data using NMO equations, neural networks and regridding inversion” submitted by Amber Camille Kelter in partial fulfilment of the requirements for the degree of Master of Science.

Abstract

To gain a better understanding of the earth's subsurface anisotropy should be considered. This thesis aims to quantify the anisotropy parameters, ε and δ, that define compressional and converted waves. It is investigated whether a better approximation can be found from inversion of compressional wave data, converted wave data or the use of these in conjunction. A synthetic data set is used to develop and evaluate a number of inversion algorithms that estimate ε and δ. Algorithms include NMO equations, neural networks and regridding inversion. Neural networks are the most robust when applied to compressional wave data. In particular, it is found that δ is best estimated using P-wave neural networks that solve for δ, while ε is best estimated using P-wave neural networks that solve for both ε and δ.

Having attained quality results from the synthetic data set, the optimal inversion techniques are applied to the Blackfoot data set. The results are encouraging and consistent with that of Elapavuluri (2000) and Thomsen (1986) where the coals and shales displayed a greater degree of anisotropy than the sands.

Acknowledgements

John C. Bancroft
Kevin Hall
Hang Xing
Helen Issac
Kim Munro
Friends
CREWES

Table of Contents

List of Tables

List of Figures

Chapter 1 Introduction

1.1 Introduction

The most basic technique of exploration geophysics consists of sending seismic waves into the subsurface and recording the reflected energy at the surface using receivers. Processing the reflected energy allows the shapes and characteristics of underground structures to be identified and to assist in the prediction of the presence or absence of petroleum and/or minerals. In petroleum exploration two commonly invoked techniques are the seismic reflection method and vertical seismic profiling (VSP).

Many models in exploration seismology naively presume that the earth is isotropic, that is, seismic velocities do not vary with direction. Yet individual crystals and most common earth materials are observed to be anisotropic with elastic parameters that vary with orientation (Shearer, 1999). Thus, it would be surprising if the earth was entirely isotropic. Further, it is now commonly accepted that most upper crustal rocks are anisotropic to some extent (Crampin, 1981) and more recently it has become apparent that anisotropy is evident in many other parts of the earth (Shearer, 1999). Alternating layering of high and low velocities where the thickness of the layer is less than the wavelength of the seismic signal will also appear anisotropic.

In the past exploration seismologists and other scientists and engineers have been somewhat hesitant to consider the full effects of anisotropy. This may include several reasons such as the greater computational complexity and the lack of computing power required to estimate and apply an anisotropic correction.

I recently attended a technical talk at the 2004 annual SEG in Denver, Colorado where a memorable statement was made 'anisotropy: the rule not the exception'. I believe that this statement is a glimpse of the future where it will no longer be acceptable to dismiss anisotropic influences. Consequently, the ability to accurately define anisotropy is essential.

1.2 Background

Contributions to seismic anisotropy were pioneered by Postma (1955) who identified that a completely isotropic layered earth could appear anisotropic if the layering were on a finer scale than the wavelengths of the seismic waves. Jolly (1956) reported finding SH-waves that travelled twice as fast in the horizontal direction as in the vertical direction. Backus (1962) determined approximate equations for the variation of the P-wave velocity as a combination of elastic constants. Helbig (1964) discussed the velocity variation in media with elliptical anisotropy and Levin (1978) analysed the accuracy of the travel time equations based on derivatives. White and Sengbush (1953) discussed measuring seismic velocities at shallow depths and Berryman (1979) gave examples of shear waves having much stronger anisotropic behaviour then compressional waves.

A cornerstone paper on anisotropy was written in 1986 by Thomsen. Thomsen's paper did not initially receive the praise that it is now recognized with (Grechka, 2001). At first glance it seemed like no more than a manipulation of known equations that describe the velocities of waves propagating in a vertically transverse isotropic (VTI) media. However, in reality his now famous parameters ε, δ and γ define combinations of the elastic coefficients responsible for such commonly measured quantities as normal-

moveout (NMO) velocities and amplitude versus offset (AVO). Other significant contributions to the field have been made by Grechka et al. (1999), Alkhalifah (1994), Tsvankin et al. (1994, 1995, 1996 and 2001) and Daley et al. (1977, 1979 and 2004).

The anisotropic parameters must first be quantified in order to incorporate their effects into seismic processing. The first measurement of P-wave anisotropy was the ratio between horizontal and vertical velocities, normally ranging from 1.05 – 1.1, but sometimes as great as 1.2 (Sheriff 2002). Today Thomsen's dimensionless parameters ε, δ and γ elegantly describe anisotropy; ε and δ determine P- and SV-wave anisotropy, while γ describes SH-wave anisotropy.

Considerable research has been carried out in the extraction of ε and δ from surface seismic and borehole measurements. Most methods, including the ones used in this study, focus on moveout and traveltime equations (e.g., Alkhalifah and Tsvankin, 1995; Grechka and Tsvankin, 1998a, b; Grechka and Tsvankin, 1999; Grechka et al., 2001) or on joint compressional and converted wave studies which are also used in this study (e.g., Sayers, 1999; van der Baan and Kendall, 2002).

This thesis aims to compare and contrast methods used to recover ε and δ from surface seismic data; namely to determine if a better estimation of these parameters comes from considering P-wave data, PS-wave data or the two in conjunction. Different methods of recovering the anisotropy parameters will be investigated including NMO equations for VTI media, shifted-hyperbola NMO equations, neural networks and regridding inversion.

1.3 Motivation

Erroneous assumptions of isotropic velocity lead to flawed images and thus incorrect interpretations where targets can appear to be shifted both in depth and laterally (Isaac et al., 2004). A common observation of including anisotropy is that the velocity model will differ from the isotropic case. This has repercussions in all aspects of seismic processing; non-hyperbolic moveout is evident, DMO fails to operate on both flat and dipping events simultaneously, migration is dependant on the phase angle of the wavefront which will no longer be equivalent to the group angle and polarity reversals are seen in AVO analysis for certain combinations of Thomsen's parameters (Yilmaz, 2001). In fact, any process that involves the concept of a scalar (isotropic) velocity field is subject to error (Tsvankin and Thomsen, 1994).

1.4 Overview and my contributions

Determination of δ is straight forward, but the determination of ε is not nearly as simple. By definition, resolution of ε requires knowledge of the horizontal velocity; a parameter that is difficult to recover from surface seismic data. One inversion algorithm analyzed in this study uses offset moveout equations to estimate ε by equating like terms in their traveltime definitions. These terms are non-linear and contain more than one parameter that has to be resolved; therefore non-linear inversion techniques are required. A possible inversion technique is regridding inversion. In contrast this method is compared to results obtained with neural networks.

In the work that follows chapter 2 discusses the theoretical basis of the equations used in regridding inversion and provides an overview of the inversion techniques of regridding and neural networks.

Chapter 3 introduces synthetic modeling and the results of the anisotropic parameter estimations. I have used the synthetic ray tracing package NORSAR2D to generate a synthetic model and processed and interpreted the results using PROMAX. The resultant data are inverted for ε and δ. Evaluation of the parameter estimations are expressed in detail in chapter 3. Chapter 4 discusses inversion results after being applied to the Blackfoot data and chapter 5 discusses results and conclusions.

Appendix 1 is an overview of seismic velocities and appendix 2 discusses sensitivity analysis done on neural networks and regridding inversion.

My contributions are summed up below:

1. Created a synthetic model and decided upon physical properties using NORSAR2D software
2. Defined geometry of the survey to be ray traced
3. Generated synthetics using the anisotropic ray tracer in NORSAR2D
4. Processed and interpreted ray tracing results in PROMAX
5. Created a program in Matlab to convert RMS velocities to interval velocities
6. Created a program in Matlab that optimized neural network inversion
    a. declared type of network, number of layers, number of neurons, type of transfer functions and stopping criterion
7. Created a program in Matlab that implemented neural networks including declaration of training, target and simulation data

8. Created a program in Matlab to do regridding inversion
9. Processed Blackfoot data in PROMAX

Chapter 2 Theory

A material is anisotropic if its properties, when measured at a given location, change with direction; and is isotropic if its properties do not change with angle (Winterstein, 1990). Thus the speed of a ray propagating through an anisotropic medium depends on direction. This requires the concepts of phase and group velocities that are defined in terms of the elastic coefficients, which are in turn functions of Thomsen's anisotropy parameters. These concepts will be developed in this chapter. An overview of regridding inversion and neural networks is also provided in this chapter.

2.1 Body wave propagation

Any quantitative description of seismic wave propagation requires the characterization of internal forces and deformations in solid materials. In order to formulate the equations of motion in a homogeneous elastic anisotropic medium, it is necessary to define and formulate relative quantities such as stress and strain. Strain defines deformation while stress describes an internal force. Stress and stain do not exist independently; they are related through a constitutive relation described below in equation 2.1.

When an elastic wave propagates through rocks displacements are in accordance with Hooke's Law as formulated by Love (1927). Namely the stress and stain are related through the constitutive relation

$$\sigma_{ij} = c_{ijkl} e_{kl}, \tag{2.1}$$

where σ_{ij} is the stress tensor, c_{ijkl} the elastic (stiffness) tensor and e_{kl} the strain tensor. The elements e_{kl} of the strain tensor are defined by spatial derivatives of the displacement vector $\boldsymbol{u}$

$$e_{kl} = \frac{1}{2}\left(\frac{\partial u_k}{\partial x_l} + \frac{\partial u_l}{\partial x_k} \right). \tag{2.2}$$

The elastic tensor, c_{ijkl}, is a fourth-order tensor with 81 (3^4) independent components. However both the strain and the stress tensor are symmetric resulting in

$$c_{ijkl} = c_{jikl} = c_{ijlk}, \tag{2.3}$$

and reducing the number of independent components to 36. The potential energy, also known as the strain energy, is expressed as $E_w = \frac{1}{2}\sigma_{ij} e_{ij} = c_{ijkl} e_{ij} e_{kl}$ (Aki and Richards, 2002) where $\frac{\partial E_w}{\partial e_{ij}} = \sigma_{ij} = c_{ijkl} e_{kl}$ which implies that

$$c_{ijkl} = c_{klij}, \tag{2.4}$$

since $\frac{\partial^2 E_w}{\partial e_{ij} \partial e_{kl}} = \frac{\partial^2 E_w}{\partial e_{kl} \partial e_{ij}}$. Resulting in only 21 of these components being independent; this is the maximum number of elements required to describe an anisotropic medium (Krebes, 2003). For a transverse isotropic medium symmetry conditions further reduce the number of independent components from 21 to 5, and for the isotropic case, only 2 elastic moduli are required.

Using the Voigt recipe (Musgrave, 1970) the fourth order stiffness tensor can be rewritten as a second order symmetric matrix:

$$c_{ijkl} \Rightarrow c_{\alpha\beta}, \tag{2.5}$$

where $ij \Rightarrow \alpha$ and $kl \Rightarrow \beta$.

For a transverse isotropic medium with a vertical symmetry axis the elastic tensor is written as (Thomsen, 1986)

$$c_{\alpha\beta} = \begin{bmatrix} c_{11} & c_{11}-2c_{66} & c_{13} & 0 & 0 & 0 \\ c_{11}-2c_{66} & c_{11} & c_{13} & 0 & 0 & 0 \\ c_{13} & c_{13} & c_{33} & 0 & 0 & 0 \\ 0 & 0 & 0 & c_{44} & 0 & 0 \\ 0 & 0 & 0 & 0 & c_{44} & 0 \\ 0 & 0 & 0 & 0 & 0 & c_{66} \end{bmatrix}. \tag{2.6}$$

This tensor has five independent elastic constants that completely describe the medium. These elastic components are related to the anisotropic or Thomsen's parameters and will be developed below.

2.2 Transverse Isotropy

Frequent causes of anisotropy are

1. foliation of clay minerals
2. fine layering in sedimentary rocks
3. stress aligned fractures, cracks or pore space.

Mechanisms (1) and (2) usually give rise to a symmetry axis that is normal to the bedding; when this axis is vertical it is defined as vertical transverse isotropy (VTI). Conversely mechanism (3) has an axis parallel to the fracture or crack normal; when the normal is horizontal it is defined as horizontal transverse isotropy (HTI). Mediums

composed of combinations of VTI and HTI have an orthorhombic symmetry (Crampin et al., 1984).

In a vertically transverse isotropic medium the velocities of waves travelling in the x-z plane (offset-depth plane) vary with direction while the velocities of waves travelling in the x-y plane (transverse plane) do not. Typically waves traveling in the horizontal direction will be faster than those traveling in the vertical direction.

2.3 Phase Velocity

The phase velocities, $v(\theta)$, for three mutually orthogonal polarizations can be described in terms of the elastic constants (Thomsen, 1986). Daley and Hron (1977) give expressions for the phase velocities in terms of the elastic tensor components where the phase velocity of a compressional wave is

$$v_P(\theta) = \sqrt{\frac{c_{33} + c_{44} + (c_{11} - c_{33})\sin^2(\theta) + D(\theta)}{2\rho}}, \tag{2.7}$$

of a shear wave with a vertical polarization direction is

$$v_{SV}(\theta) = \sqrt{\frac{c_{33} + c_{44} + (c_{11} - c_{33})\sin^2(\theta) - D(\theta)}{2\rho}}, \tag{2.8}$$

and of a shear velocity with horizontal polarization is

$$v_{SH}(\theta) = \sqrt{\frac{c_{66}\sin^2(\theta) + c_{44}\cos^2(\theta)}{\rho}}, \tag{2.9}$$

where ρ is the density and $D(\theta)$ denotes

$$D(\theta) = \{(c_{33} - c_{44})^2 + 2[2(c_{13} - c_{44})^2 - (c_{33} - c_{44})(c_{11} + c_{33} - 2c_{44})]\sin^2\theta + [(c_{11} + c_{33} - 2c_{44})^2 + 4(c_{13} - c_{44})^2]\sin^4\theta\}^{1/2}. \quad (2.10)$$

It is convenient to define the non-dimensional anisotropic parameters in terms of the elastic tensor components; this simplifies equations 2.7 – 2.9. Following Thomsen (1986) the anisotropic parameters can be defined as

$$\varepsilon = \frac{c_{11} - c_{33}}{2c_{33}}, \quad (2.11)$$

$$\gamma = \frac{c_{66} - c_{44}}{2c_{44}}, \quad (2.12)$$

and

$$\delta = \frac{(c_{13} + c_{44})^2 - (c_{33} - c_{44})^2}{2c_{33}(c_{33} - c_{44})}. \quad (2.13)$$

The P-wave velocity in the direction of the symmetry axis is defined as

$$\alpha_0 = \sqrt{c_{33}/\rho}, \quad (2.14)$$

and for the S-wave velocity as

$$\beta_0 = \sqrt{c_{44}/\rho}. \quad (2.15)$$

Equations 2.11 – 2.15 constitute 5 linear equations with 5 unknowns that are solved for the elastic constants such that

$$c_{33} = \rho\alpha_0^2, \quad (2.16)$$

$$c_{44} = \rho\beta_0^2, \quad (2.17)$$

$$c_{11} = \varepsilon 2c_{33} + c_{33} = 2\rho\alpha_0^2(\varepsilon + \frac{1}{2}), \tag{2.18}$$

$$c_{66} = \gamma 2c_{44} + c_{44} = 2\rho\beta_0^2(\gamma + \frac{1}{2}), \tag{2.19}$$

and

$$\begin{aligned} c_{13} &= \sqrt{\delta 2c_{33}(c_{33} - c_{44}) - (c_{33} - c_{44})^2} - c_{44} \\ &= \rho a_0 \sqrt{\left(\alpha_0^2 - \beta_0^2\right)\left(2\delta + 1 - \beta_0^2 / \alpha_0^2\right)} - \rho\beta_0^2 \end{aligned}. \tag{2.20}$$

Substituting these into equations 2.7 - 2.9 exact solutions for the phase velocities in terms of Thomsen's parameters are found (Daley and Hron, 1977 and 2004)

$$v_p(\theta) = \alpha \sqrt{1 + \varepsilon \sin^2\theta + \frac{1}{2}\left(1 + \frac{\beta^2}{\alpha^2}\right)\left\{\sqrt{1 + \frac{4(2\delta - \varepsilon)\sin^2\theta\cos^2\theta}{1 + \frac{\beta^2}{\alpha^2}} + \frac{4\varepsilon\left(1 - \frac{\beta^2}{\alpha^2} + \varepsilon\right)\sin^4\theta}{\left(1 + \frac{\beta^2}{\alpha^2}\right)^2}} - 1\right\}}, \tag{2.21}$$

$$v_{SV}(\theta) = \beta \sqrt{1 + \frac{\alpha^2}{\beta^2}\left[\varepsilon \sin^2\theta - \frac{1}{2}\left(1 - \frac{\beta^2}{\alpha^2}\right)\left\{\sqrt{1 + \frac{4(2\delta - \varepsilon)\sin^2\theta\cos^2\theta}{1 + \frac{\beta^2}{\alpha^2}} + \frac{4\varepsilon\left(1 - \frac{\beta^2}{\alpha^2} + \varepsilon\right)\sin^4\theta}{\left(1 + \frac{\beta^2}{\alpha^2}\right)^2}} - 1\right\}\right]}, \tag{2.22}$$

$$v_{SH}(\theta) = \beta_0 \sqrt{1 + \gamma \sin^2\theta}. \tag{2.23}$$

Expanding these equations into Taylor series and neglecting higher order terms you obtain the familiar simplified solutions for the phase velocities (Thomsen, 1986) that are assumed valid under the condition of weak anisotropy:

$$v_P(\theta) = \alpha_0(1 + \delta \sin^2\theta\cos^2\theta + \varepsilon \sin^4\theta), \tag{2.24}$$

$$v_{SV}(\theta) = \beta_0 (1 + \frac{\alpha_0^2}{\beta_0^2} (\varepsilon - \delta) \sin^2 \theta \cos^2 \theta), \tag{2.25}$$

and

$$v_{SH}(\theta) = \beta_0 (1 + \gamma \sin^2 \theta). \tag{2.26}$$

These equations assume weak anisotropy meaning the absolute values of ε, δ and γ are less than 0.2. I will return to the weak anisotropic assumption in section 2.5.

2.4 Group Velocity

The x and y axes are equivalent for a transversely isotropic medium therefore we can confine ourselves to the x-z plane in the discussion of this type of medium. Figure 2-1 depicts the phase angle, θ (associated with the direction of wave propagation) and the ray or group angle, ϕ (associated with the direction of energy transport). The phase velocity is the local velocity of the wavefront in the direction perpendicular to the wavefront and is the velocity used when referring to the horizontal slowness or the ray parameter, p. In contrast, the group velocity is the velocity of the ray and governs the speed at which wave-fronts propagate.

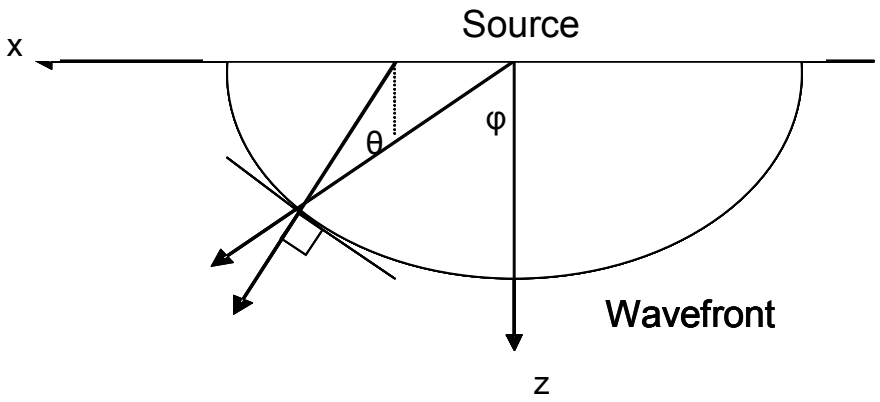

Figure 2-1 Depiction of phase angle and group angle. Angles are measured with respect to the vertical axis. The group angle resolves the direction of energy propagation while the phase angle resolves the local direction of the wavefront.

For a plane wave the phase velocity is defined as $v = \frac{\omega}{k}$ where ω is the angular frequency and k is the wave number. If $\vec{k} = k(\sin\theta\hat{x}_1 + \cos\theta\hat{x}_3)$, where $\hat{x}_1$ is a unit vector pointing in the x-direction and similarly $\hat{x}_3$ is a unit vector pointing in the z-direction, then the phase velocity as a function of the angle is given by

$$v(\theta) = \frac{\omega}{k}(\sin\theta\hat{x}_1 + \cos\theta\hat{x}_3), \tag{2.27}$$

(Aki and Richards, 2002). However it is the group velocity, the velocity at which the energy propagates, that would be measured at a geophone. The group velocity is defined as $V(\phi) = \frac{d\omega}{dk}$ or in terms of the phase velocity as

$$V(\phi) = \left(v\sin\theta + \frac{dv}{d\theta}\cos\theta\right)\hat{x}_1 + \left(v\cos\theta - \frac{dv}{d\theta}\sin\theta\right)\hat{x}_3. \tag{2.28}$$

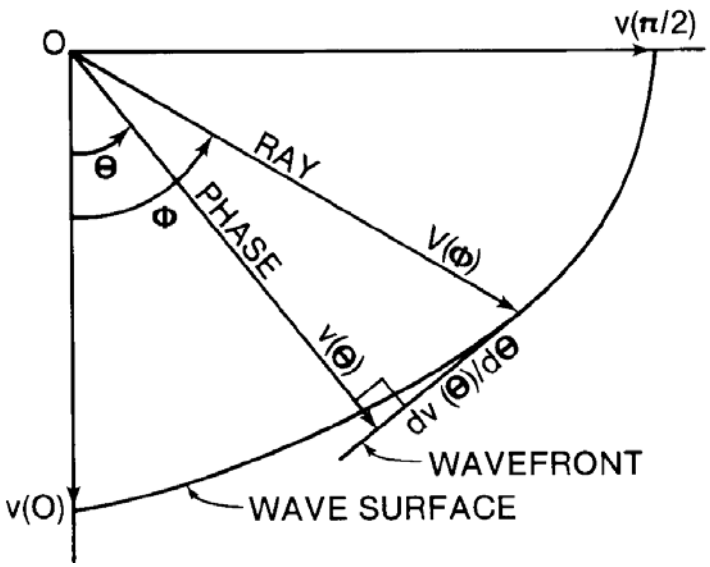

Figure 2-2 Depiction of group and phase velocity directions diverging from a point source. (Byun, 1984)

The group and phase velocities are illustrated in Figure 2-2. From Byun (1984) it can be shown that

$$v(\theta) = V(\phi)\cos(\phi - \theta), \tag{2.29}$$

$$\tan(\phi - \theta) = \frac{1}{v(\theta)}\frac{dv(\theta)}{d\theta}, \tag{2.30}$$

and

$$V^2(\phi) = v^2(\theta) + \left(\frac{dv}{d\theta}\right)^2. \tag{2.31}$$

Therefore, the magnitude of the group velocity can be defined in terms of the phase velocity and the phase angle. The application of the trigonometric identity

$$\tan(x - y) = \frac{\tan(x) - \tan(y)}{1 + \tan(x)\tan(y)}, \tag{2.32}$$

to equation 2.30 is necessary to express the group angle, ϕ as

$$\phi = \tan^{-1}\left[\frac{\tan(\theta)+\frac{1}{v(\theta)}\frac{dv(\theta)}{d\theta}}{1-\frac{1}{v(\theta)}\frac{dv(\theta)}{d\theta}\tan(\theta)}\right]. \tag{2.33}$$

We have now successfully defined the phase velocity and its angle and the group velocity and its angle in an anisotropic medium.

2.5 Weak Anisotropic Approximation

Thomsen (1984) introduced an approximation to the methods described previously go from phase velocity in equations 2.24, 2.25 and 2.26 to group velocity and corresponding group angle. He stated that a sufficient linear approximation is

$$V(\phi) \approx v(\theta), \tag{2.34}$$

and that the group angle could be solved from a linear approximation to equation 2.33 (Thomsen, 1986)

$$\tan(\phi) = \tan(\theta)\left[1+\frac{1}{\sin(\theta)\cos(\theta)}\frac{1}{v(\theta)}\frac{dv}{d\theta}\right]. \tag{2.35}$$

This leads to group angles for the P and two S-waves defined as

$$\tan(\phi_P) = \tan(\theta)\left[1+2\delta+4(\varepsilon-\delta)\sin^2(\theta)\right], \tag{2.36}$$

$$\tan(\phi_{SV}) = \tan(\theta)\left[1+2\frac{\alpha_0^2}{\beta_0^2}(\varepsilon-\delta)(1-2\sin^2(\theta))\right], \tag{2.37}$$

and

$$\tan(\phi_{SH}) = \tan(\theta)(1+2\gamma)\,. \tag{2.38}$$

Solving for the group velocities using equation 2.31 and neglecting higher order terms the linear approximation goes as

$$\begin{aligned} V_P(\phi) &= v_p(\theta) \\ V_{SV}(\phi) &= v_{SV}(\theta)\,, \\ V_{SH}(\phi) &= v_{SH}(\theta) \end{aligned} \tag{2.39}$$

thereby validating equation 2.34. The above formulae states that at a given ray angle ϕ, the corresponding phase angle can be calculated from equations 2.36 - 2.38, then equations 2.24 – 2.26 and 2.39 may be used to find the corresponding group velocity.

2.6 Normal Moveout (NMO)

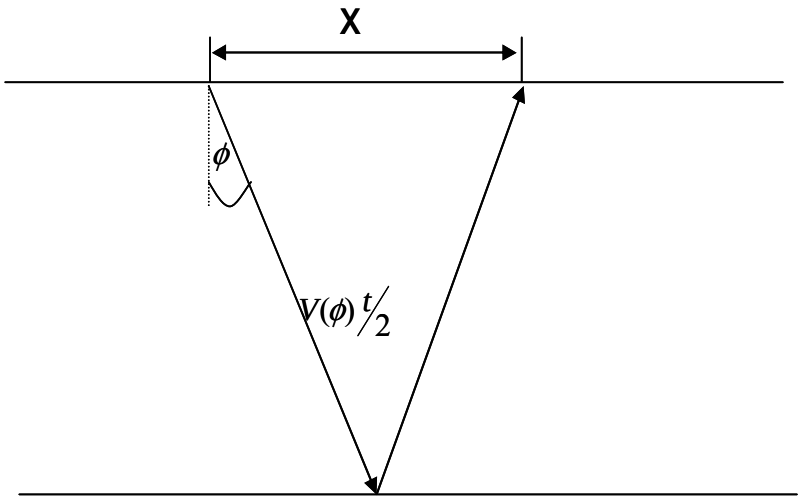

Figure 2-3 Conventional reflection survey. The distance that the down going wave travels is noted on that arm of the ray.

Consider a conventional reflection survey in a homogeneous anisotropic elastic medium (Figure 2-3), the traveltime can be computed from

$$\left[V(\phi)\frac{t(\phi)}{2}\right]^2 = \left[V(0)\frac{\tau}{2}\right]^2 + \left(\frac{x}{2}\right)^2, \tag{2.40}$$

where τ is the vertical (zero-offset) two-way traveltime, x the source receiver offset, t the travel time from source to reflector to receiver, $V(0)$ the vertical velocity and $V(\phi)$ the velocity for incident angle ϕ. When t^2 is solved for we obtain

$$t^2(\phi) = \left[\frac{V(0)}{V(\phi)}\right]^2\left[\tau^2 + \frac{x^2}{V^2(0)}\right]. \tag{2.41}$$

Equation 2.41 is dependent upon ϕ and forms a curved line in the $t^2 - x^2$ plane. The slope of this line is given by first rearranging equation 2.41 and then invoking the quotient rule for the derivative as evaluated below

$$\begin{aligned} t^2 &= \frac{V(0)^2\tau^2 + x^2}{V(\phi)^2}, \\ \frac{dt^2}{dx^2} &= \frac{V^2(\phi) - \left(V(0)^2\tau^2 + x^2\right)\dfrac{dV(\phi)^2}{dx^2}}{V(\phi)^4}, \\ \frac{dt^2}{dx^2} &= \frac{1}{V^2(\phi)} - \frac{t^2}{V(\phi)^2}\frac{dV(\phi)^2}{dx^2}. \end{aligned} \tag{2.42}$$

This can be further expressed according to Thomsen (1986) as

$$\frac{dt^2}{dx^2} = \frac{1}{V^2(\phi)}\left[1 - \frac{2\cos^2\phi}{V(\phi)}\frac{dV(\phi)}{d\sin^2(\phi)}\right]. \tag{2.43}$$

The normal moveout velocity is defined using the initial slope of this line where $V_{nmo}^2(\psi) = \lim_{x\to 0} \frac{dx^2}{dt^2}$ and ψ is the dip angle of the reflector. The ray parameter, p, can be incorporated into this equation to ease its computational complexity to resolve

$$V_{NMO}^2(\psi) = \frac{2}{\tau} \lim_{x\to 0} \frac{dh}{dp}, \tag{2.44}$$

where $h = x/2$ or the half-offset of the source and receiver (Tsvankin, 1995). Letting z_0 be the depth of the zero-offset reflection point then $h = z_0 \tan(\phi)$ and equation 2.44 becomes

$$V_{NMO}^2(\psi) = 2\frac{z_0}{\tau} \lim_{x\to 0} \frac{d\tan(\phi)}{dp}. \tag{2.45}$$

To evaluate equation 2.45 the general relations between the group and phase velocities demonstrated above are used. First we express $\frac{d\tan(\phi)}{dp} = \frac{d\tan(\phi)}{d\theta}\frac{d\theta}{dp}$. Referring to equation 2.33 we see

$$\frac{d\tan\phi}{d\theta} = \frac{1 + \frac{1}{v}\frac{d^2v}{d\theta^2}}{\cos^2\theta\left(1 - \frac{\tan\theta}{v}\frac{dv}{d\theta}\right)^2}, \tag{2.46}$$

and since $p = \sin(\theta)/v$ by Snell's law

$$\frac{d\theta}{dp} = \frac{v}{\cos\theta(1 - \frac{\tan\theta}{v}\frac{dv}{d\theta})}, \tag{2.47}$$

then

$$\frac{d\tan(\phi)}{dp} = \frac{v\left(1+\frac{1}{v}\frac{d^2v}{d\theta^2}\right)}{\cos\theta\left(1-\frac{\tan\theta}{v}\frac{dv}{d\theta}\right)^3}. \tag{2.48}$$

Letting $z_o = \frac{1}{2}V(\phi)t\cos\phi$ and using the expression for the group velocity in equation 2.28 and recalling that the phase angle, θ, for the zero-offset ray is equal to the dip angle, ψ, z_0 becomes

$$z_0 = \frac{1}{2}V(\psi)t\cos\psi\left(1-\frac{\tan\psi}{V(\psi)}\frac{dv}{d\theta}\right). \tag{2.49}$$

The NMO velocity is obtained by substituting equations 2.48 and 2.49 into 2.45

$$V_{NMO}(\psi) = \frac{V(\psi)}{\cos(\psi)}\frac{\sqrt{1+\frac{1}{V(\psi)}\frac{d^2v}{d\theta^2}}}{\left(1-\frac{\tan\psi}{V(\psi)}\frac{dv}{d\theta}\right)}, \tag{2.50}$$

where the derivatives of the phase velocity are evaluated at the dip angle, ψ, of the reflector. Difficulties are anticipated when implementing this equation for shear waves that have cusps or singularities. The expression in equation 2.50 is fairly simple to invoke because it only involves the phase velocity function and the components of the group velocity. For a flat reflector the normal moveout velocities evaluate as

$$V_{NMO}(0,P) = V_{p0}\sqrt{1+2\delta}, \tag{2.51a}$$

$$V_{NMO}(0,P-SV)=V_{p0}\sqrt{\frac{1+\,1/\gamma_c}{1+\gamma_o}}\,, \tag{2.51b}$$

where $\gamma_c=\gamma_0\left(\frac{1+2\delta}{1+2\sigma}\right), \gamma_0=\frac{V_{p0}}{V_{s0}}$ and $\sigma=\frac{V_{p0}^2}{V_{s0}^2}(\varepsilon-\delta)$ (Tsvankin and Thomsen, 1994 and Thomsen, 1999). Note that σ reduces to zero for both isotropic (ε = 0, δ = 0) and elliptically anisotropic (ε = δ) (Daley and Hron, 1979) media. The equations for V_{NMO} are equal to the RMS velocities when the anisotropic parameters (σ, δ and γ) are all zero.

2.7 Reflection travel times

A common approximation to reflection moveout is the Taylor series expansion of the $t^2(x^2)$ curve near $x^2=0$ (Taner and Koehler, 1969)

$$t_T^2=A_0+A_2x^2+A_4x^4+\ldots, \tag{2.52}$$

where $A_0=\tau^2$, $A_2=\left[\frac{dt^2}{dx^2}\right]_{x=0}$ and $A_4=\left[\frac{1}{2}\frac{d}{dx^2}\left(\frac{dt^2}{dx^2}\right)\right]_{x=0}$. Tsvankin and Thomsen (1994) expressed these coefficients for a P-wave in a VTI medium as

$$A_2(P)=\frac{1}{V_{P0}^2(1-2\delta)}$$

$$, \tag{2.53}$$

$$A_4(P)=\frac{-2(\varepsilon-\delta)}{\tau_{P0}^2V_{P0}^4}\frac{1+\dfrac{2(\varepsilon-\delta)}{1-V_{S0}^2/V_{p0}^2}}{(1+2\delta)^4}$$

and for the P-SV case as

$$A_2(P-SV)=\frac{1}{V_{p0}^2\left(\frac{1+1/\gamma_c}{1+\gamma_o}\right)}$$

$$A_4(P-SV)=\frac{\frac{-1}{1+\gamma_c}\left[2\frac{(\varepsilon-\delta)}{1+2\delta}\frac{\left(\gamma_0^2-1\right)}{\gamma_0}\gamma_c^2+\frac{\left(\gamma_2^2-1\right)^2}{4(\gamma_0+1)}\right]}{V_{nmo\_P-SV}} \quad , \qquad (2.54)$$

where γ_2 is the V_p/V_s moveout ratio as defined in equations 2.51a and 2.51b. The short spread moveout velocity is expressed through A_2 as $V_{NMO}=1/\sqrt{A_2}$.

2.8 Shifted hyperbola NMO (SNMO) traveltime

In 1956 Bolshix derived an equation for NMO in a layered earth. Malovichko (1978, 1979) unaware of an error is Bolshix's formulation developed an equation for the shifted hyperbola NMO by realising that Bolshix equation approximated Gauss's hypergeometric series, which has a known analytical sum (Castle, 1994).

In 1994 Castle obtained the approximation to the NMO equation, the shifted hyperbola (SNMO)

$$t^2=t_0(1-S)+\sqrt{\left(\frac{t_o}{S}\right)^2+\frac{x^2}{SV_{rms}^2}}\,. \qquad (2.55)$$

Geometrically this equation describes a hyperbola that is symmetric about the t-axis and has asymptotes that intersect at $\left(x=0,t=t_0\left(1-\frac{1}{S}\right)\right)$. Essentially it is a Dix NMO curve

shifted in time by $t_0\left(1-\frac{1}{S}\right)$ (Castle, 1994). The shift parameter, S is a constant and equivalent to

$$S=\frac{\mu_4}{\mu_2^2}, \tag{2.56}$$

where μ_2 and μ_4 are the second and fourth order time weighted moments of the velocity distribution defined from $\mu_j=\frac{\sum_{k=1}^{N}\tau_k V_k^j}{\sum_{k=1}^{N}\tau_k}$ where V_k is the interval velocity of the k^{th} layer and τ_k the vertical traveltime through the k^{th} layer. Equation 2.55 can be written in the form of Taner and Koehler (1969) where

$$A_2=\frac{1}{V_{nmo}^2}, \tag{2.57}$$

and

$$A_4=\frac{1}{4}\frac{(1-S)}{t_0^2 V_{nmo}^4}. \tag{2.58}$$

Expressions for A_2 and A_4 found in equations 2.53, 2.54, 2.57 and 2.58 are the equations used for inversion purposes.

2.9 Anisotropy Parameters

Having developed equations for the traveltime in a VTI media the following sections provide a physical understanding of the anisotropy parameters. For most sedimentary rocks, the parameters ε, γ and δ are of the same order of magnitude and usually less than 0.2; furthermore for most rock types the anisotropy parameters are positive (Thomsen, 1986). However it is possible to have negative values for the anisotropy parameters (Thomsen, 1986). In the modelling that follows the anisotropy parameters are pushed to their limits to explore the boundaries of "common" rock types.

2.9.1 Epsilon, ε

A physical meaning for the anisotropic parameters ε can be developed when considering the special case of horizontal incidence. By letting the angle θ equal 90 degrees in equation 2.24 we obtain

$$\varepsilon = \frac{v(90) - v(0)}{v(0)}, \tag{2.59}$$

where $v(90)$ is the horizontal P-wave velocity and $v(0)$ the vertical P-wave velocity. This parameter is a measure of the anisotropic behaviour of a rock and a measure of the fractional difference between the horizontal and vertical velocities. When a seismic wave propagates through a TI medium at angles nearly perpendicular to the symmetry axis the parameter ε dominates the P-wave velocity (Brittan et al, 1995). The parameter ε can also be used in combination with δ to relate group and phase velocities in a TI medium.

2.9.2 Delta, δ

It is more difficult to gain a physical understanding of δ other than to say that it is a critical factor that controls the near vertical response and that it determines the shape of the wavefront (Thomsen, 1986). If in equation 2.24 we let the angle θ equal 45 degrees and invoke equation 2.59 for ε, δ evaluates as

$$\delta = 4\left[\frac{v(\pi/4)}{v(0)} - 1\right] - \left[\frac{v(\pi/2)}{v(0)} - 1\right]. \tag{2.60}$$

When an incident P-wave propagates approximately parallel to the axis of symmetry the parameter δ dominates the anisotropic response. It is not a function of the velocity normal to the symmetry axis and can take on both positive and negative values (Brittan et al, 1995). The parameter δ may be used to relate the group and phase angles and subsequently the group and phase velocities within an anisotropic medium and is the controlling parameter for the normal moveout of compressional waves in a horizontally layered medium.

2.10 Common Scatter Point Gathers

In the recovery of ε and δ common scatter point (CSP) gathers are used. Elapavuluri (2000) showed that CSP gathers give more accurate results when inverting for the anisotropic parameters than do CMP gathers. Thus in the following velocity analysis is performed on CSP gathers.

A scatter point is defined as a point in the subsurface that scatters energy in all directions. A reflector can be approximated by an array of scatter points. It is assumed that energy from a source is scattered by all scatter points to all receivers. A common

scatter point gather is a pre-stack gather that collects all the input traces that contain energy from a vertical array of scatter points (Bancroft, 2004).

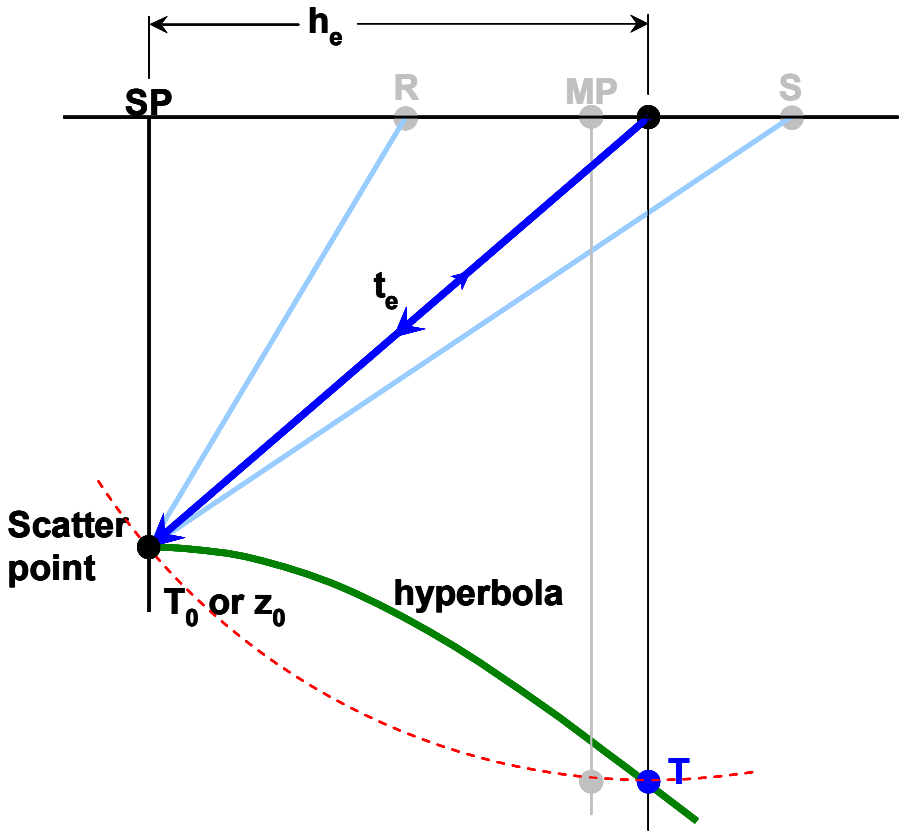

Figure 2-4 Ray paths to a scatter point and the equivalent offset, where SP is indicative of the scatter point position on the surface, R the receiver position, S the source position and MP the midpoint between the source and receiver. To and Zo define the location of the scatter point on a time or depth section respectively. T and h_e define the position of a point that will be summed into a CSP gather on a time section. (Bancroft, 2004)

All input traces may be summed into a CSP gather at an offset defined by the equivalent offset and are therefore not limited by the source receiver offset as is the case with CMP gathers. The maximum equivalent offset, h_e, is limited by the recording time (Bancroft, 2004). The equivalent offset is defined using ray paths to and from the scatter point where the source and receiver are collocated preserving traveltime. The traveltime is defined by the double square root (DSR) equation

$$t = \left[\frac{t_0^4}{4} + \frac{(x+h)^2}{V^2}\right]^{1/2} + \left[\frac{t_0^4}{4} + \frac{(x-h)^2}{V^2}\right]^{1/2}, \tag{2.61}$$

where h is half the distance from source to receiver or the midpoint referred to in CMP gathers. The collocated source and receiver travel time is given by

$$t = 2\left[\frac{t_0^2}{4} + \frac{h_e^2}{V^2}\right]^{1/2}, \tag{2.62}$$

where h_e is now the equivalent offset. Equating equations 2.61 and 2.62 the equivalent offset evaluates as

$$h_e^2 = x^2 + h^2 - \frac{4x^2h^2}{t^2V^2}. \tag{2.63}$$

Using this equivalent offset an input point can be summed into a CSP gather.

In the case of converted waves the scatter point is referred to as a conversion scatter point.

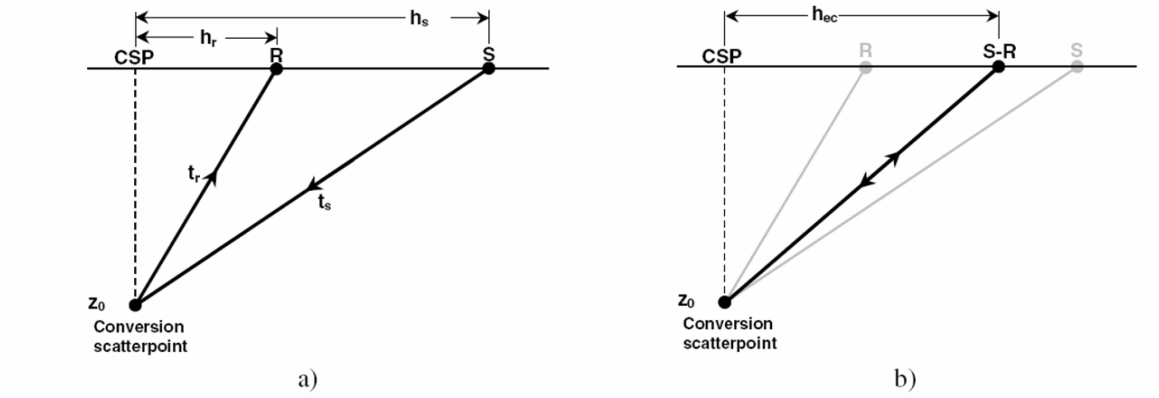

Figure 2-5 Depiction of energy reflected to and from a conversion scatter point in a) the source and receiver are not collocated in b) the source and receiver have been collocated preserving traveltime (Bancroft and Wang, 2000).

The traveltime of the ray paths in Figure 2-5 is

$$t = \frac{\left(z_0^2 + h_s^2\right)^{1/2}}{V_p} + \frac{\left(z_0^2 + h_r^2\right)^{1/2}}{V_s} = \frac{\left(z_0^2 + h_{ec}^2\right)^{1/2}}{V_p} + \frac{\left(z_0^2 + h_{ec}^2\right)^{1/2}}{V_s} = \left(\frac{1+\gamma}{V_p}\right)\left(z_0^2 + h_{ec}^2\right)^{1/2} = \sqrt{\tau^2 + \frac{4h_{ec}^2}{V_{ps}^2}}\,. \quad (2.64)$$

The depth z_o is a pseudo depth from a time section, h_s is the distance from CSP to source, h_r the distance from CSP to receiver, $\gamma = V_p/V_s$ and h_{ec} the distance from the conversion scatter point to the collocated source and receiver

$$h_{ec} = \left\{\left[\frac{\gamma}{\gamma+1}\left(z_0^2 + h_s^2\right)^{1/2} + \frac{\gamma}{\gamma+1}\left(z_0^2 + h_r^2\right)^{1/2}\right]^2 - z_0^2\right\}^{1/2}. \quad (2.65)$$

CSP velocity analysis is founded on the distances from sources and receivers to the CSP location where as CMP velocity analysis is based solely on the source receiver offsets. Additional benefits of CSP gathers include easier picking of velocities in structurally complex areas, better signal to noise ratio and after an NMO correction has been applied the section will be prestack migrated (Bancroft, 2004).

2.11 Neural Network

The first of two non-linear inversion algorithms invoked for this study is now discussed. An artificial neural network (ANN) is an information processing algorithm that is inspired by the way biological nervous systems, such as the brain, process information. In the simplest sense a neural network is a mathematical algorithm that can be trained to solve a problem. The key element is the novel structure of the information processing system. It is composed of a large number of highly interconnected processing elements (neurons) working in unison to solve specific problems (Haykin, 1999).

Artificial neural networks, like people, learn by example. An ANN is configured for a specific application, such as pattern recognition or data classification, through a learning process. The learning process in biological systems involves adjustments to the synaptic connections that exist between the neurons. This is true of ANNs as well. In the work that follows ANN's are referred to simply as neural networks or NN.

Neural networks, with their remarkable ability to derive meaning from complicated or imprecise data, can be used to extract patterns and detect trends that are too complex to be noticed by either humans or other computer techniques (Freeman et al 1991). A trained neural network can be thought of as an 'expert' in the category of information it has been given to analyse.

2.11.1 Backpropagation

Backpropagation feedforward networks are utilized in this study. The architecture of such an algorithm is shown below in Figure 2-6.

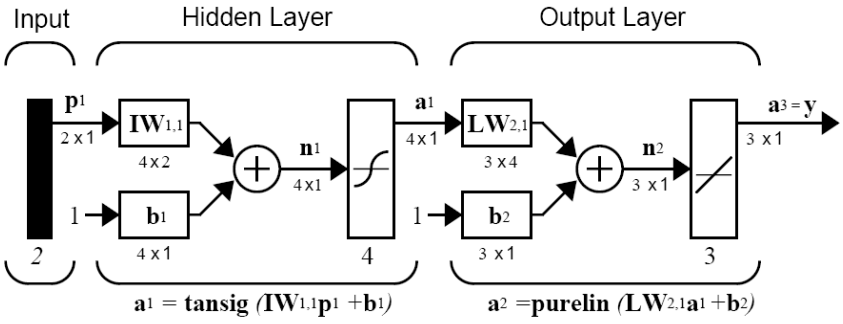

Figure 2-6 Feedforward neural network architecture. (Matlab help documentation)

This architecture uses backpropagation to train the network elements. In the backpropagation algorithm input vectors and the corresponding output target vectors are used to train a network until it can approximate a function. Networks with biases, a

sigmoid layer (hidden layer) and a linear layer (output layer) are capable of approximating any function with a finite number of discontinuities (Higham and Higham, 2000). In Figure 2-6 there are 2 elements in the input vector, four neurons in the hidden layer and three elements in the output/target vector. During training the weights (IW,LW) and biases (b) of the network are iteratively adjusted to maximize the network.

Data are trained in batch mode where the weights and biases of the network are updated only after the entire training set has been applied to the network. In the application of the back propagation algorithm two distinct passes of computation are performed; first a forward pass and second a backward pass (Haykin, 1999; Freeman and Skapura, 1991). In the forward pass the synaptic weights remain unaltered throughout the network and the function signals, appearing at the output of every neuron, of the network are computed on a neuron by neuron basis. The output is compared with the desired response obtaining an error signal. In summary the forward pass begins at the first hidden layer by presenting it with the inputs and terminates at the output layer by computing the error signal (difference between the output and target values) for each neuron in this layer. The backward pass, on the other hand, starts at the output layer by passing the error signals leftward through the network, layer by layer, and recursively computing the local gradient in weight space for each neuron such that a correction is computed for the weights that is proportional to the partial derivatives. The basic procedure is embodied in the following summarized by Freeman et al. (1991):

1. Apply an input vector to the network and calculate the corresponding output values

2. Compare actual outputs with the correct outputs and determine a measure of the error
3. Determine in which direction to change each weight in order to reduce the error
4. Determine the amount by which to change the weight
5. Apply the corrections to the weights
6. Repeat 1-5 with all training samples until the error is reduced to an acceptable value.

Sensitivity analysis was preformed on this algorithm where error was added to the velocity and the resultant anisotropy parameters were resolved. Details are contained in Appendix 2. Error in the calculated δ is linearly proportional to errors in the input velocity, errors in the calculated ε where not linearly proportional to errors in the velocity. Further δ was observed to be more susceptible to error when the velocity was erroneous.

2.12 Regridding Inversion

The second non-linear inversion algorithm used in this study is regridding inversion. In a regridding inversion algorithm multiple unknown parameters are estimated to evaluate a function with a known solution, velocity in this case. Initially a guess at the range of possible values for the unknown parameters is made. In this sense the unknowns are discretized. The ensuing function is evaluated at each point. Figure 2-7 illustrates the error surface and picks. The true solution is marked by a red asterisk. After this first iteration the optimal solutions is marked by a black asterisk. The area around this optimal solution is further discretized into a finer grid and again the function is

evaluated. This regridding is continued until the estimated solution is within a specified tolerance of the real solution; thereby obtaining estimates of the unknown parameters. The final solution is marked by a green square. Sensitivity analysis was also performed on this algorithm and is presented in Appendix 2. Error was added to δ, the shift parameter and the velocity independently and the consequent ε evaluated. Errors in the calculated ε were linearly proportional to errors in the input parameters and layer dependant. It is found that the regridding inversion is most sensitive to errors in the velocity.

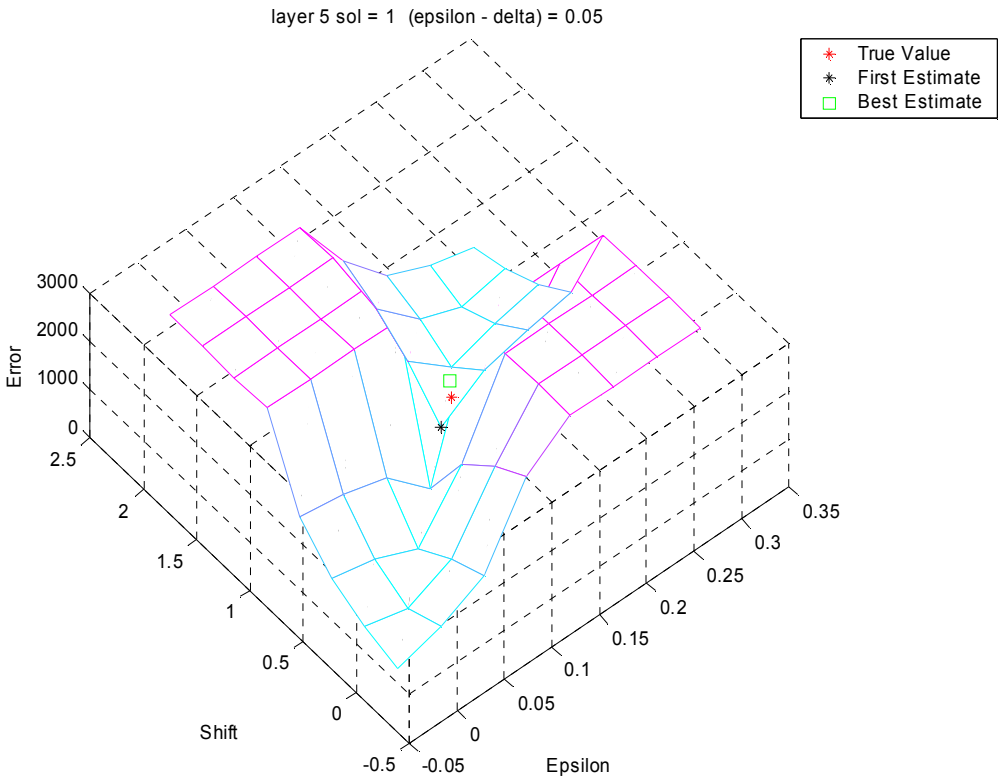

Figure 2-7 A function to be optimized is evaluates for a range of possible values for each parameter. The area around the best solution is then further discretized into a finer grid and the function revaluated obtaining a new optimal solution.

An anticipated hurdle is the phenomenon of non-uniqueness. The system is underdetermined and therefore a unique solution may not exist. This is circumvented by evaluating the gradient of the error. When ε is greater than or equal to δ it is found that the best solution is obtained by discretizing the area with the steepest gradient conversely when δ is greater than ε the flattest area is discretized.

Chapter 3 Synthetic Modelling

Methods developed in the previous chapters are applied to a synthetic data set to recover ε and δ. A 2-D anisotropic model was created and ray traced in the depth domain using NORSAR2D software, a ray tracing package, to generate synthetic seismic sections. These sections were imported into PROMAX, a seismic processing package, to extract RMS velocities that were manipulated to obtain apparent ε and δ values. Methods invoked to recover the anisotropic parameters include:

1. P-wave NMO equations estimating δ
2. P-wave regridding inversion using NMO equations estimating ε
3. PS-wave regridding inversion using NMO equations estimating ε
4. PS-wave regridding inversion using NMO equations estimating ε and δ
5. Neural networks applied to P-wave data estimating δ
6. Neural networks applied to P-wave data estimating ε
7. Neural networks applied to P-wave data estimating δ and ε
8. Neural networks applied to PS-wave data estimating δ
9. Neural networks applied to PS-wave data estimating ε
10. Neural networks applied to PS-wave data estimating δ and ε
11. Neural networks applied to PP- and PS-wave data estimating δ
12. Neural networks applied to PP- and PS-wave data estimating ε
13. Neural networks applied to PP- and PS-wave data estimating δ and ε

The details of each method will be discussed below.

3.1 Building the Model

Synthetic seismograms are generated by NORSAR2D from the following steps

1. Build the geological model
    a. Define layer boundaries
    b. Define material properties
2. Specify geometry of the survey
3. Simulate the survey (ray tracing)
4. Convolve ray tracing results with a wavelet to generate synthetic seismograms

3.1.1 Geological Model

The synthetic model consists of nine horizontal layers each with its own unique material properties. The model was 20.0 km long and 6 km deep. The thinnest layer was 0.25 km and the thickest 1.0 km.

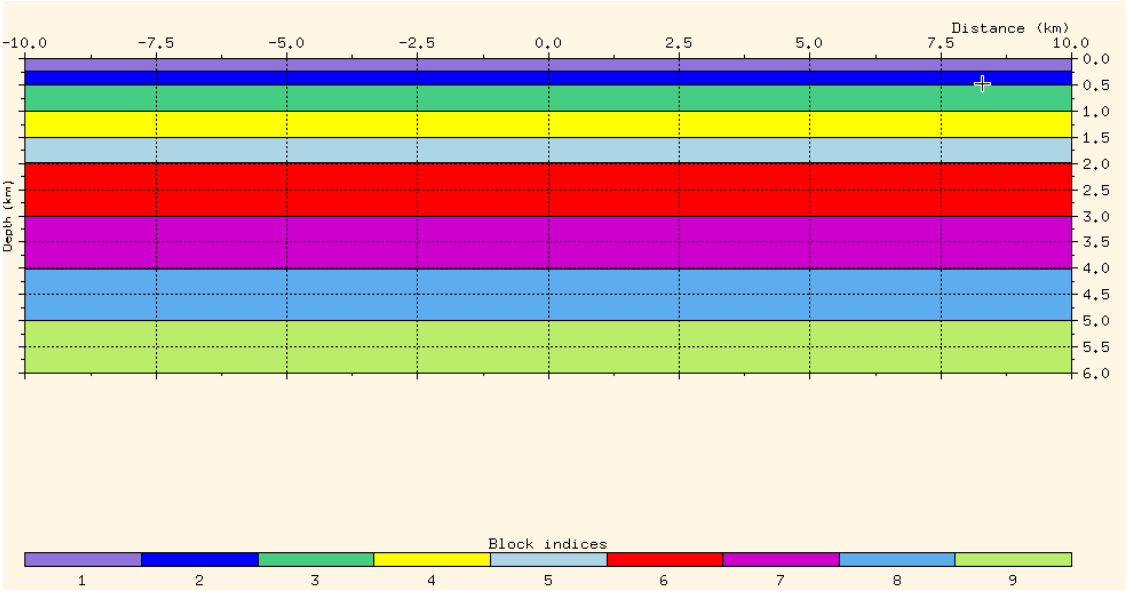

Figure 3-1 Geological model used to create synthetic seismic section. Model consists of 9 horizontal layers each with unique material properties

The material properties: P-wave velocity, S-wave velocity, density, ε and δ were assigned for each block as listed in Table 3-1.

Table 3-1 Material properties of the synthetic model

Layer	P-wave Velocity	S-wave Velocity	Density	ε	δ
	(m/s)	(m/s)	(kg/m^3)	(unitless)	(unitless)
1	1000	500	1.1	0	0.2
2	1200	600	1.2	0.05	0.25
3	1500	750	1.3	0.1	0.3
4	2000	1000	1.5	0.15	0.1
5	2500	1250	1.7	0.2	0.15
6	3000	1500	1.9	0.25	0.2
7	4000	2000	2.2	0.3	0.25
8	5000	2500	2.4	0.2	0.3
9	6500	3250	2.6	0.1	0.3

3.1.2 Seismic Survey

Two seismic surveys were simulated using the model to produce synthetics; a PP- and a PS-survey. For both surveys, the shot spacing was 60.0 m and the receiver spacing 20.0 m. In total there were 300 receivers and 234 shots with all receivers reading all shots. A very simplified version of the survey is seen in Figure 3-2.

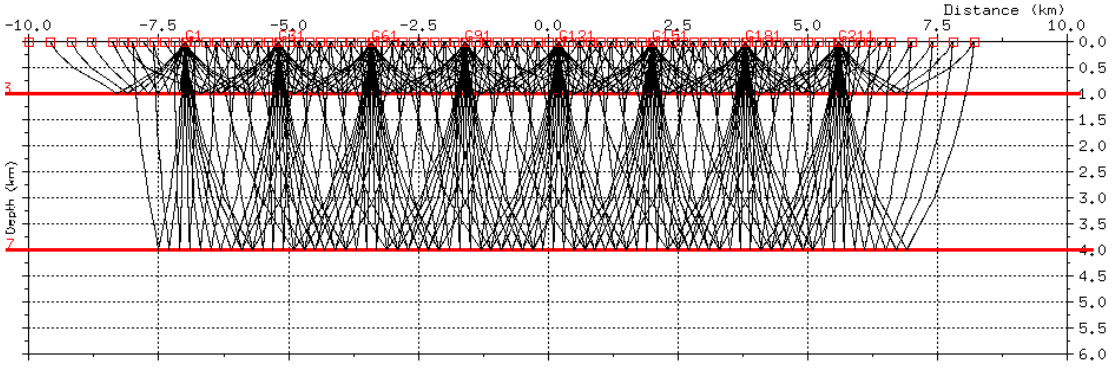

Figure 3-2 A simplified example of ray tracing results using NORSAR2D's anisotropic ray tracer.

3.1.3 Ray Tracing

Seismic ray theory is analogous to optical ray theory and has been applied for over 100 years to aid in interpreting seismic data (Shearer, 1999). It continues to be used almost extensively due to its simplicity and applicability to a wide range of problems. Ray tracing is a process by which one can calculate quantities tied to seismic wave propagation through a layered medium and may be classified as a high frequency solution to the seismic wave equations. For the high frequency approximation to hold seismic wavelengths must be shorter than the finest details of the model (Norsar 2D user guide).

Derivation of the ray tracing equations closely mimics Margrave (2002). Figure 3-3 is given as a reference for equation development.

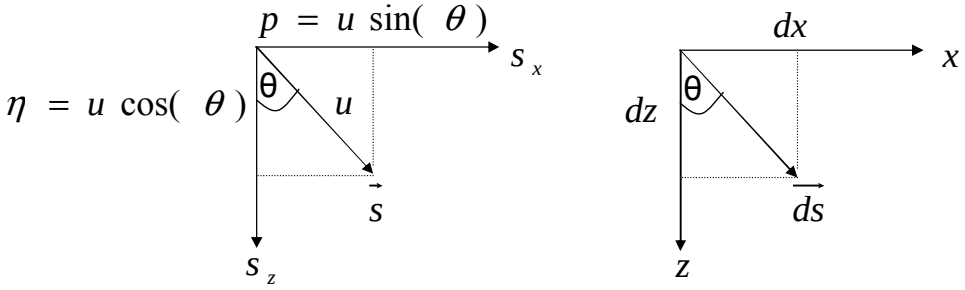

Figure 3-3 Components of the slowness vector in the slowness and x-z domain.

Integral equations will be developed to compute the travel time and distance along a particular ray. At any point along a ray the slowness vector s can be resolved into its horizontal and vertical components. The length of s is given by u. The vertical slowness η can be defined in terms of the horizontal slowness p as

$$\eta = \left(u^2 - p^2\right)^{1/2}. \tag{3.1}$$

Defining $\frac{dx}{ds} = \sin\theta = \frac{p}{u}$ and $\frac{dz}{ds} = \left(1 - \sin^2\theta\right) = \frac{\left(u^2 - p^2\right)^{1/2}}{u}$ from the chain rule we obtain

$\frac{dx}{dz} = \frac{dx/ds}{dz/ds} = \frac{p}{\left(u^2 - p^2\right)^{1/2}}$. This can be integrated to attain

$$x = p\int_{z_1}^{z_2} \frac{dz}{\left(u^2(z) - p^2\right)^{1/2}}. \tag{3.2}$$

A similar expression can be developed for time. Where $dt = uds$ and

$\frac{dt}{dz} = \frac{dt/ds}{dz/ds} = \frac{u^2}{\left(u^2 - p^2\right)^{1/2}}$ integrating we get

$$t = \int_{z1}^{z2} \frac{u^2(z)}{\left(u^2(z) - p^2\right)^{1/2}} dz. \tag{3.3}$$

Equations 3.2 and 3.3 define the general expressions used for ray tracing.

3.1.4 Synthetic Generation

Synthetic seismograms are created by convolving the ray tracing results with a damped 40 Hz minimum phase Ricker wavelet. The thinnest layer in the model is 0.5 km thick and has a velocity of 1000 m/s. The seismic wavelet is 25m in this interval thus ensuring that the high frequency assumption is not violated. The results of this convolution are stored in a SEGY file. The outcome for one of the shot gathers near the center of the line is displayed in Figure 3-4.

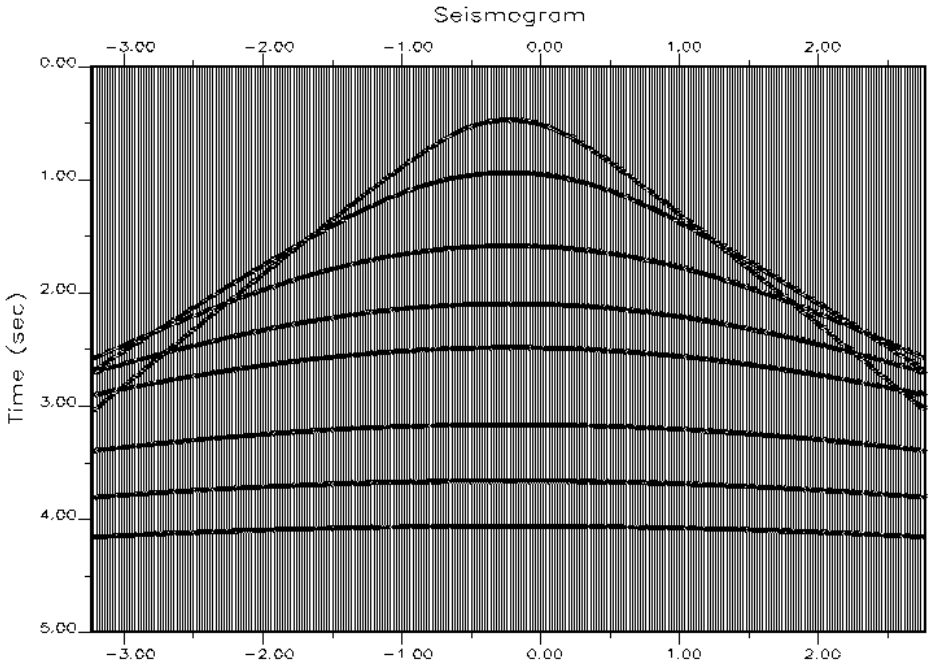

Figure 3-4 A shot gather that result from convolving the ray tracing with a Ricker wavelet.

3.1.5 RMS (stacking) Velocity Estimation

The SEGY files described above were imported into PROMAX and a basic processing flow applied as below

1. Geometry set-up
2. AGC (automatic gain control)
3. Sorting into CSP gathers
4. Velocity Analysis

A few CSP gathers were formed at selected locations using crude velocities and these gathers used to estimate more accurate velocities.

3.2 Parameter estimation

The anisotropy parameters can be estimated from the synthetic modeling. I present results from the individual data sets estimating each parameter separately as follows

1. Solving for δ from PP data
2. Solving for ε from PP data
3. Solving for δ from PS data
4. Solving for ε from PS data
5. Solving for δ using joint PP & PS data
6. Solving for ε using joint PP & PS data

and will summarize the results for ε and δ estimation at the end of this section.

Velocities used in these algorithms are interval velocities. RMS stacking velocities were found from semblance analysis in PROMAX and converted to interval velocities using Dix type integration (Appendix 1). Ratio difference refers to the difference between the true and calculated values using $ratio\ difference = \frac{abs(true - calculated)}{true}$. When calculating the ratio difference for ε only layers 2-8 are considered as the true ε value of layer 1 is zero and this leads to instability from division by zero. It is assumed that the vertical velocities (Vp(0) and Vs(0)) are readily available from VSP or sonic log data or in this case the synthetic data set.

A summary of the parameters used in neural networks is provided in Table 3-2.

Table 3-2 Summary of parameters used in neural networks

Data Type	Output	Number of Neurons	Training Inputs	Transfer Functions
PP	δ	29	Vp(0), Vs(0), Vp_int	Tan-sigmoid, Linear
PP	δ,ε	88	Vp(0), Vs(0), Vp_int	Tan-sigmoid, Linear
PP	ε	32	Vp(0), Vs(0), Vp_int, δ	Linear, Linear
PS	δ	9	Vp(0), Vs(0), Vps_int	Tan-sigmoid, Linear
PS	δ,ε	3	Vp(0), Vs(0), Vps_int	Tan-sigmoid, Linear
PS	ε	4	Vp(0), Vs(0), Vps_int, δ	Tan-sigmoid, Linear
PP & PS	δ	2	Vp(0), Vs(0), Vp_int, Vps_int	Log-sigmoid, Linear
PP & PS	δ,ε	30	Vp(0), Vs(0), Vp_int, Vps_int	Log-sigmoid, Linear
PP & PS	ε	62	Vp(0), Vs(0), Vp_int, Vps_int, δ	Linear, Linear

The number of neurons and type of transfer functions were chosen by varying the combination of transfer functions and the number of neurons (from 1 to 150) and selecting the combination that gave the lowest root mean squared (RMS) error. As a further QC step, to ensure that the neural networks were running properly, data from layers 1, 3, 5 and 7 of the geological model were chosen as training data and a simulation performed all 8 layers. Results from this training and simulation are seen in Figure 3-5, where the resultant δ for each layer is plotted. Trained results are those from training the network and simulated from applying the trained network to the data. Data used for training is a set of 'true' values and data used for simulation are values found from modeling. Discrepancies between trained and simulated values are a result of velocity picking errors.

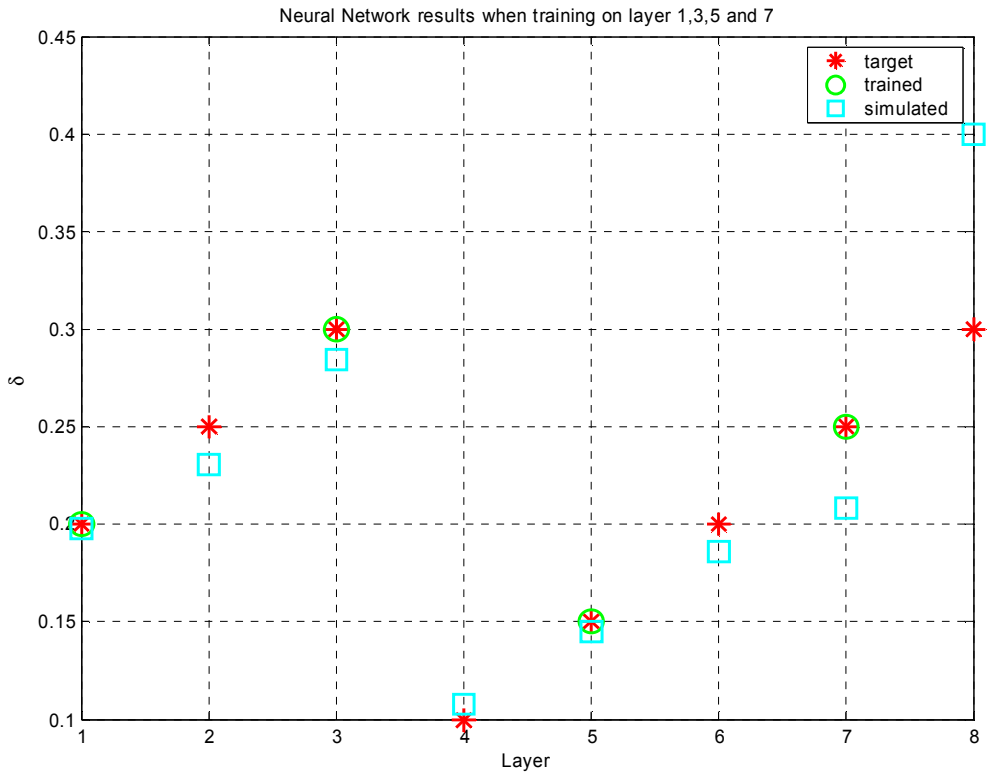

Figure 3-5 A QC check when the network is trained on layers 1, 3, 5 and 7 and then incorporated to recover results for all layers.

3.2.1 Solving for δ from PP data

For the PP survey δ values were found from three different methods

1. applying NMO equation 2.51a (PP NMO δ)
2. neural network inversion estimating δ (PP NN estimating δ)
3. neural network inversion estimating ε and δ (PP NN estimating δ and ε)

Results are listed in Table 3-3.

Table 3-3 True and estimated values of δ after applying P-wave inversion methods

Layer	Interval Velocity	True δ	PP NMO δ	PP NN Estimating δ	PP NN Estimating δ and ε
1	1180.9	0.2	0.197	0.198	0.198
2	1458.9	0.25	0.239	0.242	0.242
3	1880.1	0.3	0.286	0.288	0.290
4	2178	0.1	0.093	0.096	0.092
5	2835	0.15	0.143	0.146	0.142
6	3523.8	0.2	0.190	0.195	0.191
7	4794.8	0.25	0.218	0.237	0.233
8	6382.3	0.3	0.315	0.305	0.303

Figure 3-6 shows these results in a graphical format while Figure 3-7 displays the ratio difference as defined previously

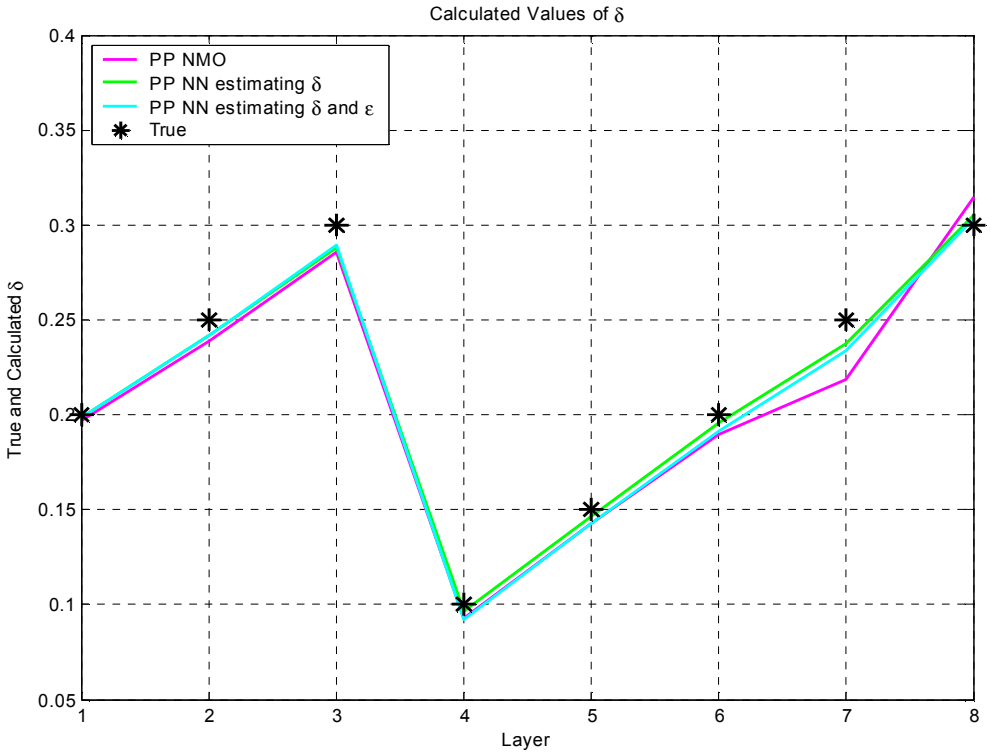

Figure 3-6 True and estimated values of δ after applying P-wave inversion methods. The neural network (NN) methods slightly outperform the NMO method.

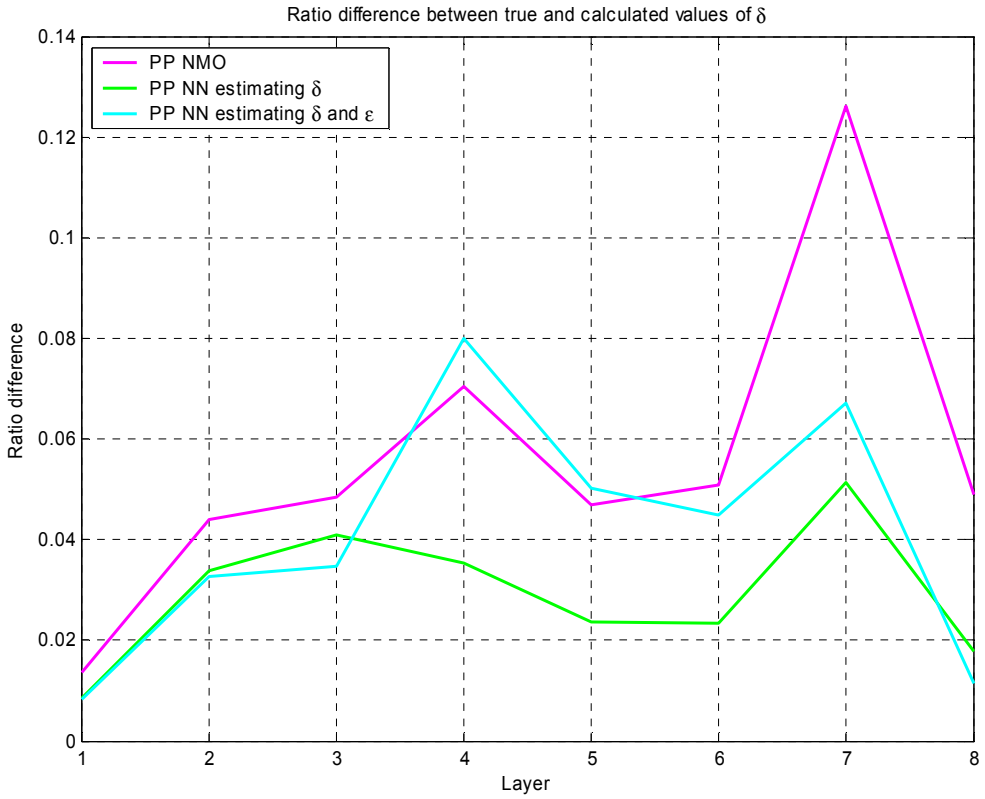

Figure 3-7 Comparison of the ratio difference between the true and calculated values of δ from P-wave inversion methods. Neural networks used to estimate δ give the most accurate results.

Table 3-4 lists the RMS errors associated with each method.

Table 3-4 Root mean squared errors of P-wave inversion methods used to estimate δ.

Method	PP NMO δ	PP NN Estimating δ	PP NN Estimating δ and ε
RMS	0.0148	0.0076	0.0091

The superior of these methods appears to be the neural networks when solving for δ.

3.2.2 Solving for ε from PP data

The parameter ε was estimated from P-wave data in three different ways

1. regridding inversion (PP Regrid ε)

equating equations 2.53 and

a. **(2.58**2.58 and solving for the interval velocity by estimating the shift parameter and ε

2. neural network inversion estimating ε (PP NN estimating ε)
3. neural network inversion estimating ε and δ (PP NN estimating δ and ε)

The regridding inversion used δ that was previously solved for from the NMO equation, equation 2.51a. Numerical results are listed in Table 3-5. The results and ratio differences are also plotted in Figure 3-8 and Figure 3-9 respectively.

Table 3-5 Results for ε using P-wave inversion methods

Layer	True ε	Regrid ε	PP NN Estimating ε	PP NN Estimating ε and δ
1	0	0.008	-0.010	0.00
2	0.05	0.060	0.046	0.051
3	0.1	0.067	0.094	0.103
4	0.15	0.165	0.143	0.146
5	0.2	0.208	0.226	0.196
6	0.25	0.218	0.263	0.247
7	0.3	0.310	0.342	0.311
8	0.2	0.264	0.170	0.169

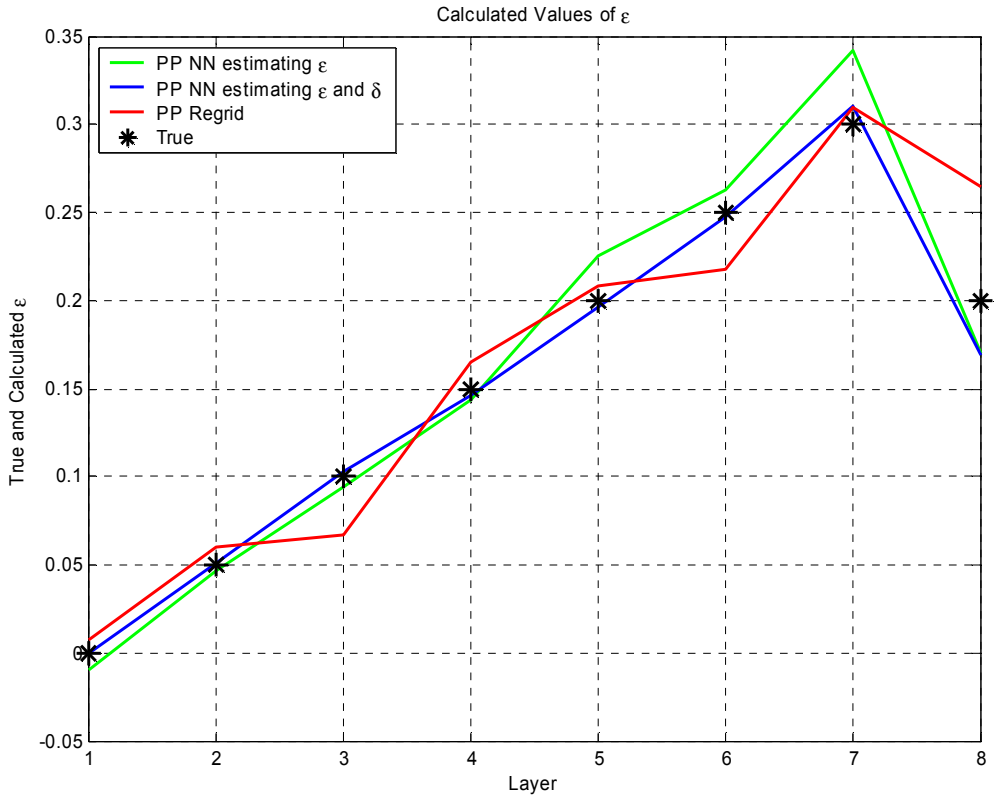

Figure 3-8 True and calculated ε values from P-wave inversion methods.

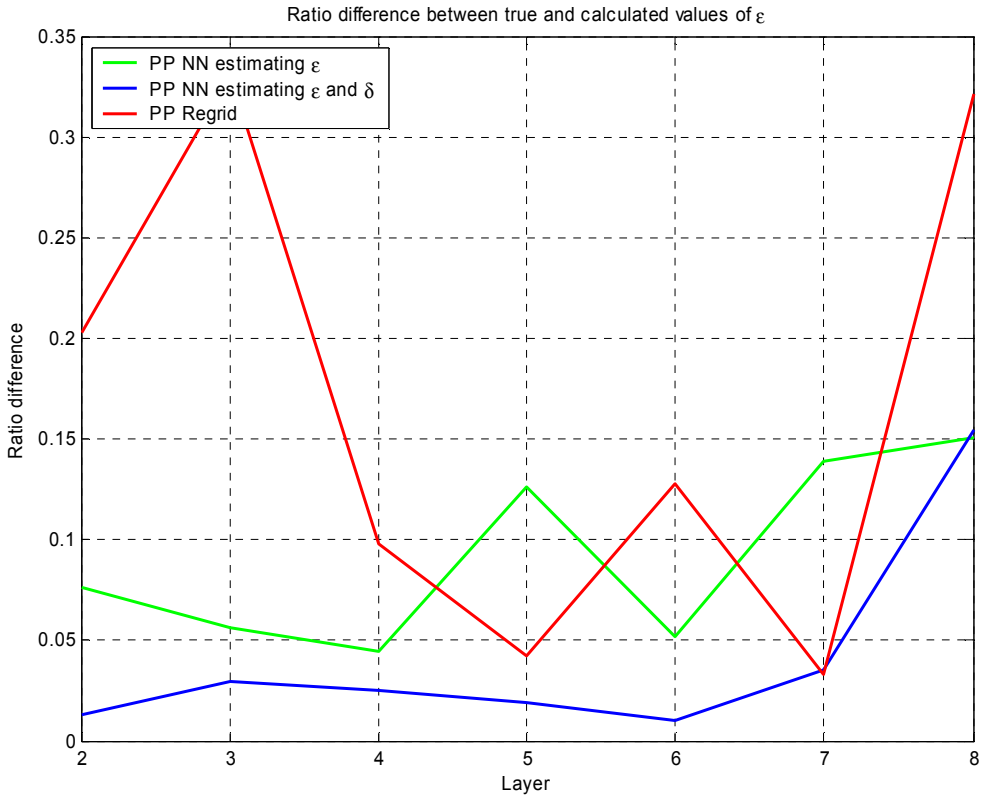

Figure 3-9 Ratio differences between true and calculated ε values calculated from P-wave inversion methods.

The RMS errors for the above methods are listed in Table 3-6.

Table 3-6 Root mean squared errors of P-wave inversion methods used to estimate ε.

Method	PP regrid ε	PP NN Estimating ε	PP NN Estimating ε and δ
RMS	0.029	0.021	0.012

The above figures and tables indicate that neural networks appear to be the superior method for recovering ε and when the neural network solves for both ε and δ the results are better than when only ε is solved for.

3.2.3 Solving for δ from PS data

Solving for δ from converted wave data was accomplished through

1. regridding inversion (PS Regrid δ)
    a. Estimating ε and δ in equation 2.51b
2. neural network inversion estimating δ (PS NN estimating δ)
3. neural network inversion estimating ε and δ (PS NN estimating δ and ε)

In equation 2.51b an initial guess for δ was obtained from the P-wave NMO equation, equation 2.51a, and the neighbourhood of this value discretized. Results are displayed in Figure 3-10 and Figure 3-11 and tabulated in Table 3-7. The corresponding RMS errors are listed in Table 3-8.

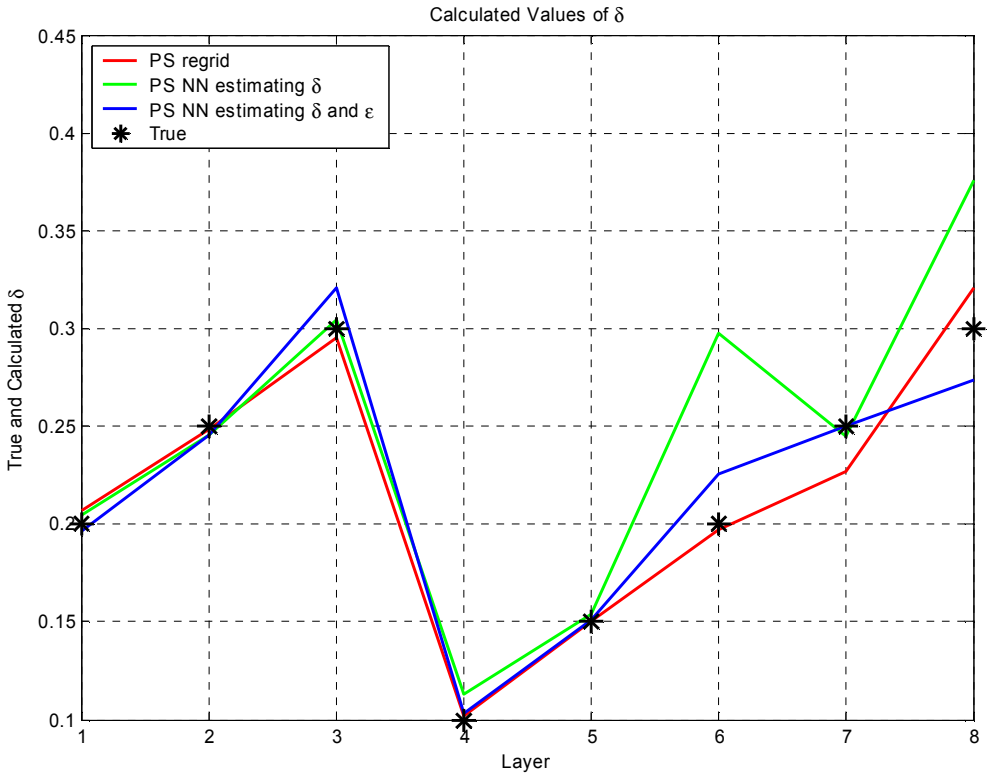

Figure 3-10 True and calculated δ values from PS-wave inversion methods.

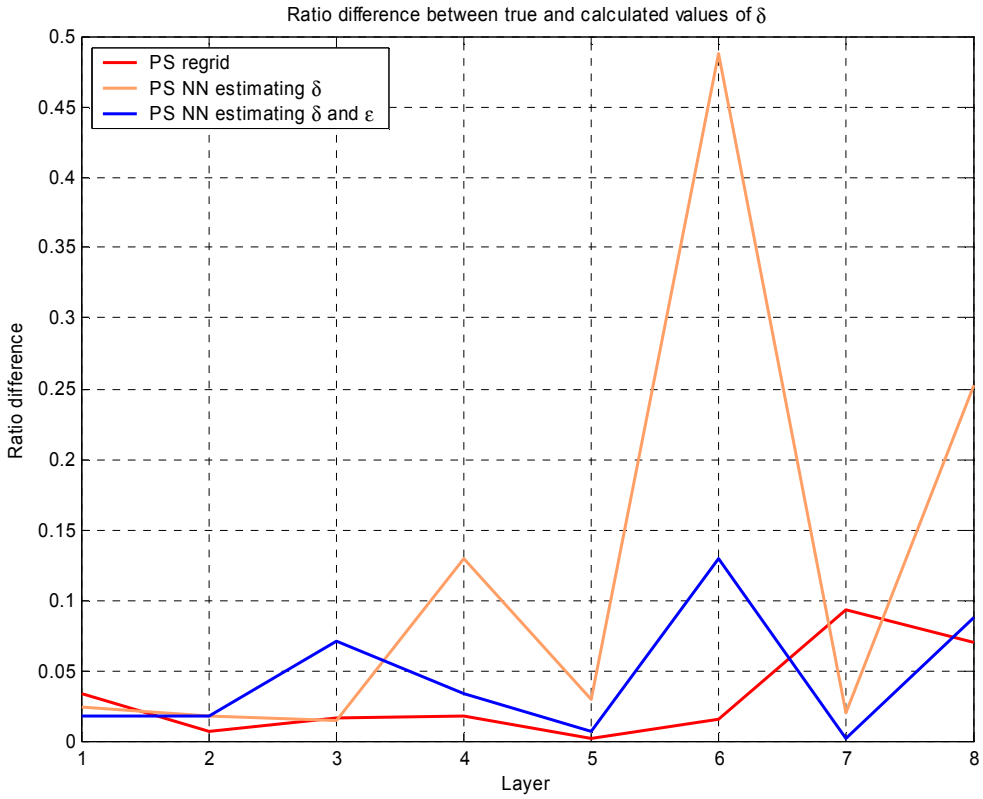

Figure 3-11 Ratio differences of true and calculated δ values from PS-wave inversion methods

Table 3-7 True and calculated δ values from PS-wave inversion methods

Layer	Interval Velocity (m/s)	True δ	PS regrid δ	PS NN Estimating δ	PS NN Estimating ε and δ
1	513.9	0.2	0.207	0.205	0.197
2	629.2	0.25	0.248	0.246	0.246
3	762.2	0.3	0.295	0.304	0.321
4	1448.6	0.1	0.102	0.113	0.103
5	1788.7	0.15	0.150	0.154	0.151
6	2072	0.2	0.197	0.298	0.226
7	2798.4	0.25	0.227	0.245	0.2497
8	3068.7	0.3	0.321	0.376	0.274

Table 3-8 RMS errors for PS-wave inversion methods used to estimate δ

Method	PS regrid δ	PS NN Estimating δ	PS NN Estimating ε and δ
RMS	0.0115	0.0441	0.0152

Of the PS-wave inversion methods used to recover δ, graphically and statistically, the regridding inversion method gives the best results.

3.2.4 Solving for ε from PS data

Solving for ε from PS-wave data was performed using four methods:

1. applying NMO equation 2.51b (PS NMO ε)
2. regridding inversion (PS Regrid ε)
    a. Estimating ε and δ in equation 2.51b
3. neural network inversion estimating ε (PS NN estimating ε)
4. neural network inversion estimating ε and δ (PS NN estimating ε and δ)

The PS NMO ε method uses δ estimated from the P-wave NMO equation, equation 2.51a. Results are given below in Figure 3-12, Figure 3-13, Table 3-9 and Table 3-10.

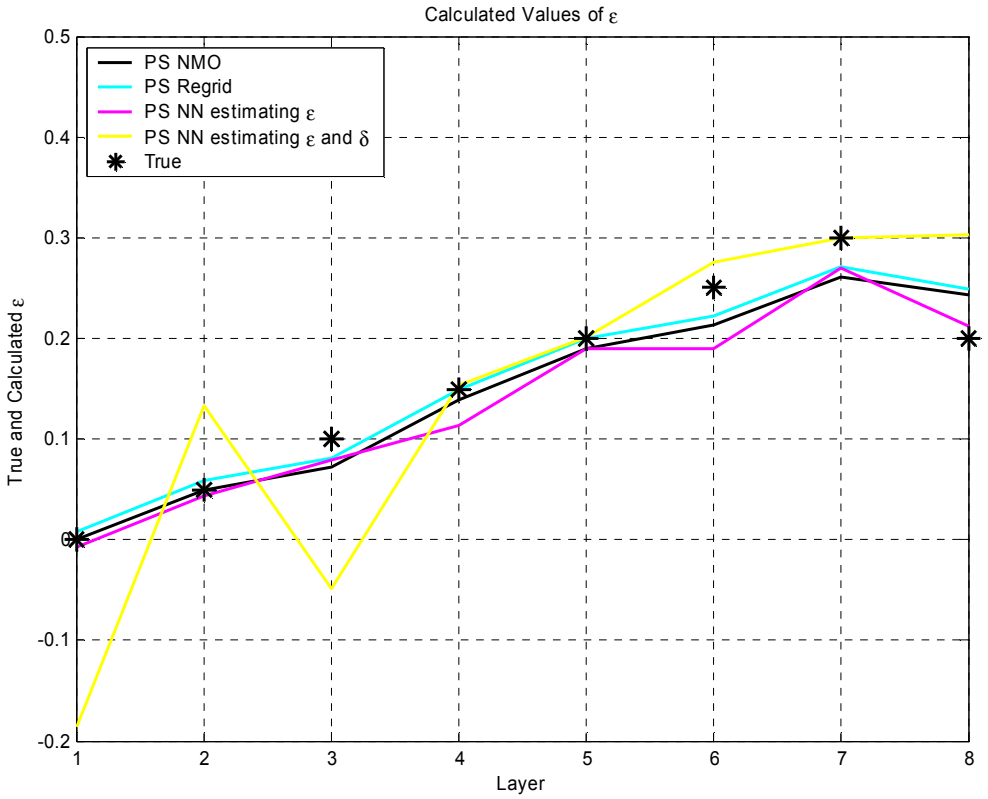

Figure 3-12 True and calculated ε values from PS-wave inversion methods.

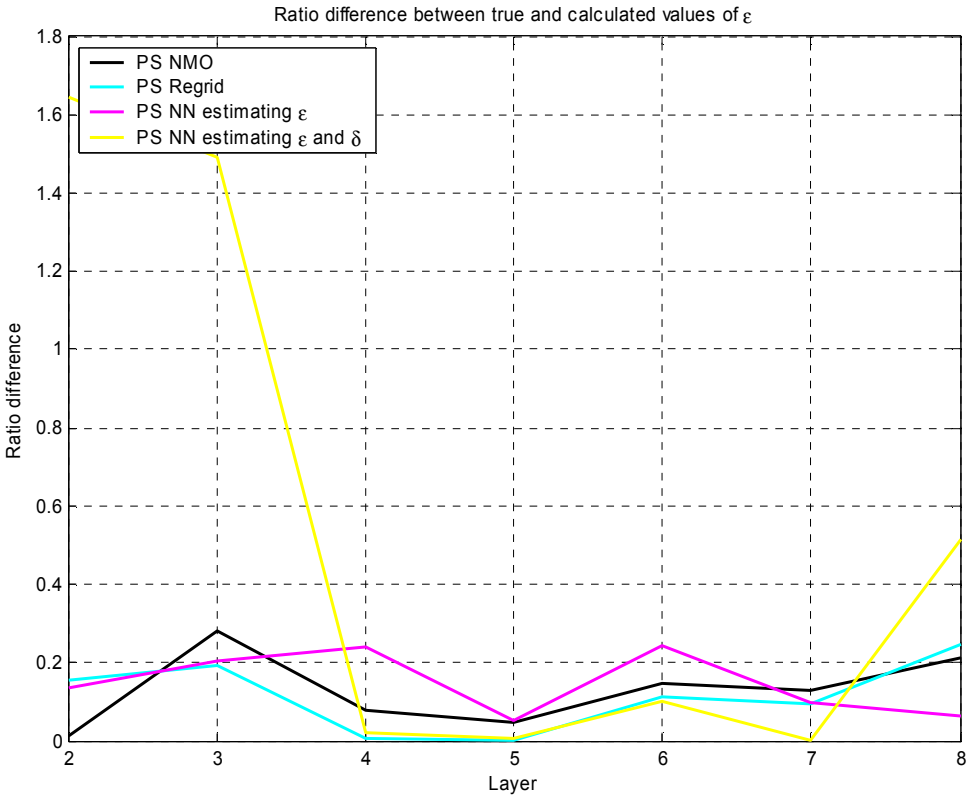

Figure 3-13 Ratio difference of calculated and true ε values calculated from PS-wave inversion methods.

Table 3-9 True and calculated ε values from PS-wave inversion methods

Layer	True ε	PS NMO ε	PS regrid ε	PS NN Estimating ε	PS NN Estimating ε and δ
1	0	-0.000	0.008	-0.007	-0.186
2	0.05	0.049	0.058	0.0431	0.132
3	0.1	0.072	0.0806	0.079	-0.049
4	0.15	0.138	0.149	0.114	0.153
5	0.2	0.190	0.199	0.190	0.201
6	0.25	0.214	0.222	0.189	0.276
7	0.3	0.262	0.272	0.270	0.300
8	0.2	0.243	0.249	0.212	0.303

Table 3-10 RMS errors PS-wave inversion methods estimating ε

Method	PS NMO ε	PS regrid ε	PS NN Estimating ε	PS NN Estimating ε and δ
RMS	0.0266	0.0238	0.0288	0.0968

Graphically and statistically the PS regridding inversion algorithm provided the best estimates of ε.

3.2.5 Solving for δ from joint PP and PS data

Both compressional wave and converted wave data were used in conjunction to investigate if better results for δ could be attained. Two types of neural networks were invoked for this task;

1. neural network inversion estimating δ (PP PS NN estimating δ)
2. neural network inversion estimating ε and δ (PP PS NN estimating ε and δ)

Results are displayed below in Table 3-11, Table 3-12, Figure 3-14 and Figure 3-15.

Table 3-11 True and calculated δ values from joint PP and PS-wave inversion methods

Layer	True δ	PP PS NN Estimating δ	PP PS NN Estimating δ and ε
1	0.2	0.208	0.190
2	0.25	0.286	0.209
3	0.3	0.213	0.333
4	0.1	0.118	0.066
5	0.15	0.149	0.152
6	0.2	0.187	0.234
7	0.25	0.250	0.250
8	0.3	0.544	0.305

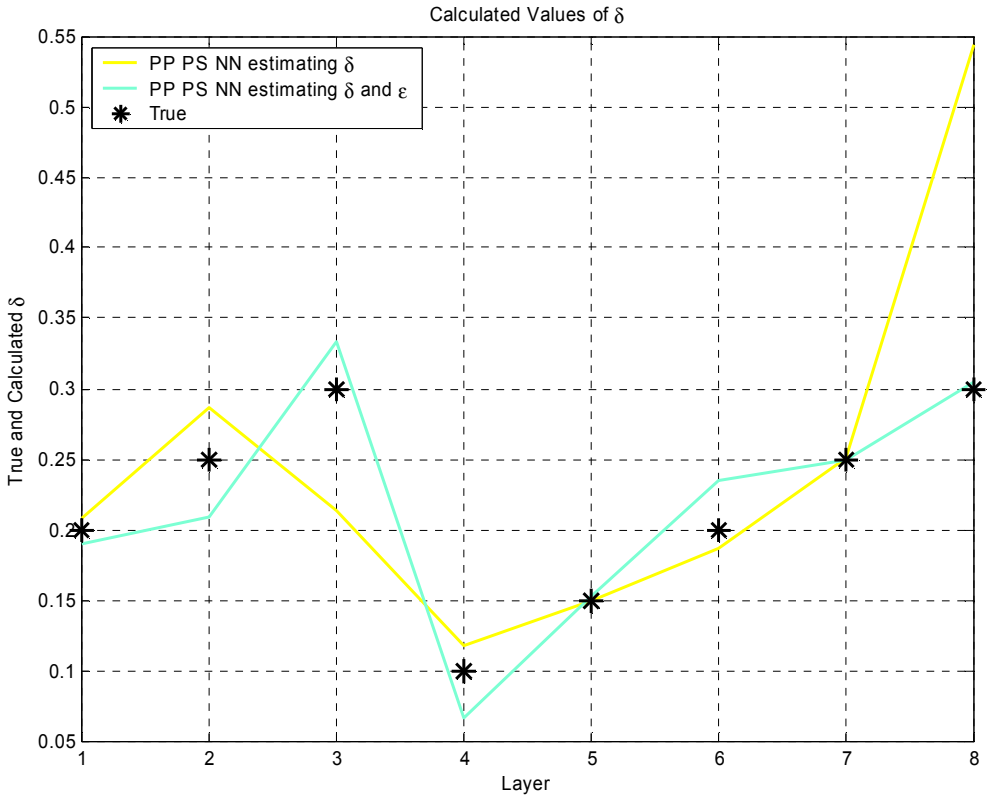

Figure 3-14 True and calculated δ values from joint PP and PS-wave inversion methods.

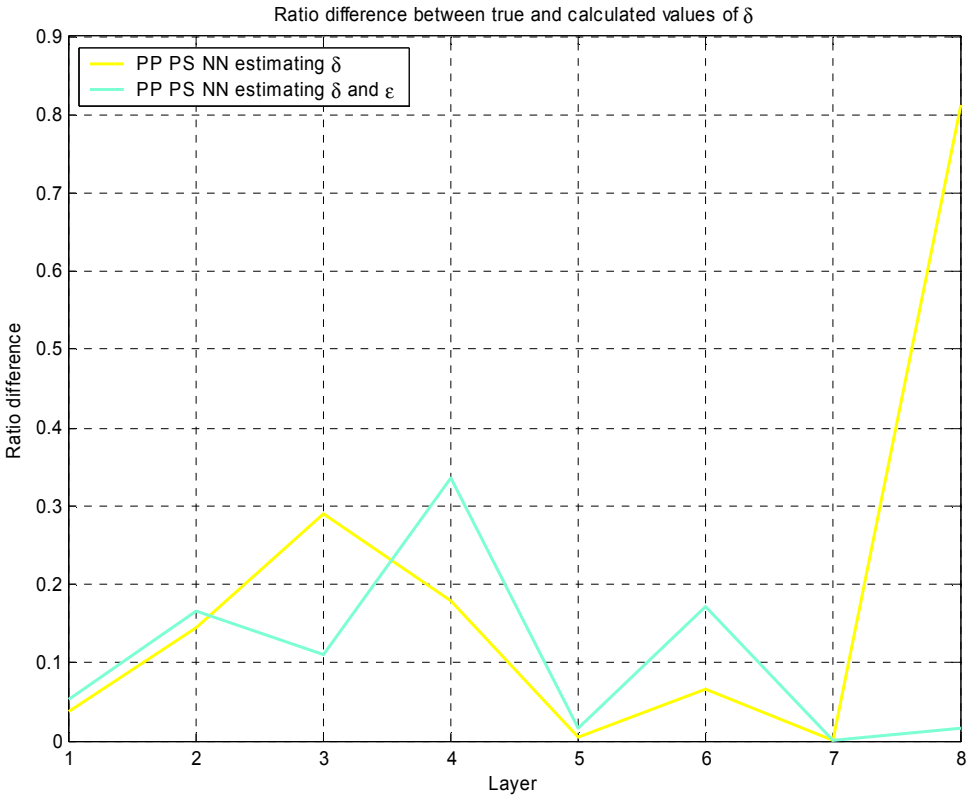

Figure 3-15 Ratio difference of calculated and true δ values calculated from joint PP and PS-wave inversion methods

Table 3-12 RMS error for joint PP and PS-wave inversion methods estimating δ

Method	PP PS NN Estimating δ	PP PS NN Estimating ε and δ
RMS	0.0929	0.0256

When both wave types are considered a neural network that solves for both parameters gives optimal results.

3.2.6 Solving for ε from joint PP and PS data

Similarly ε was determined by doing a joint inversion on compressional and converted wave data. Two types of neural networks were tested;

1. neural network inversion estimating ε (PP PS NN estimating ε)
2. neural network inversion estimating ε and δ (PP PS NN estimating ε and δ)

Results are provided in Figure 3-16, Figure 3-17, Table 3-13 and Table 3-14.

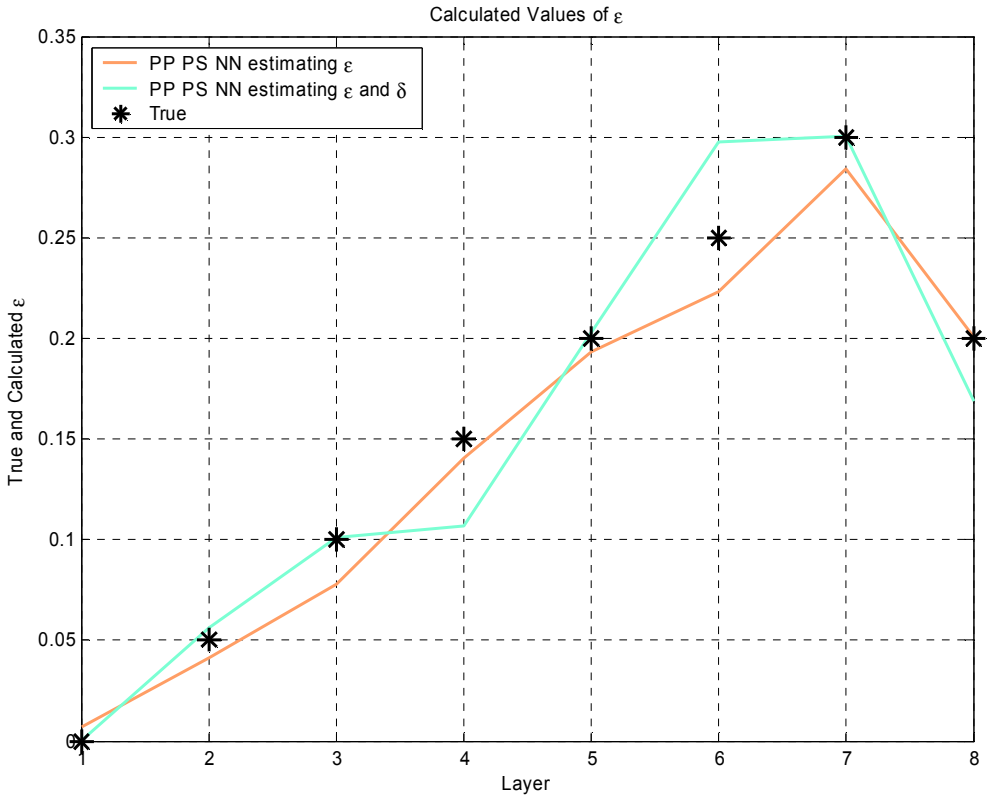

Figure 3-16 True and calculated ε values from joint PP and PS-wave inversion methods.

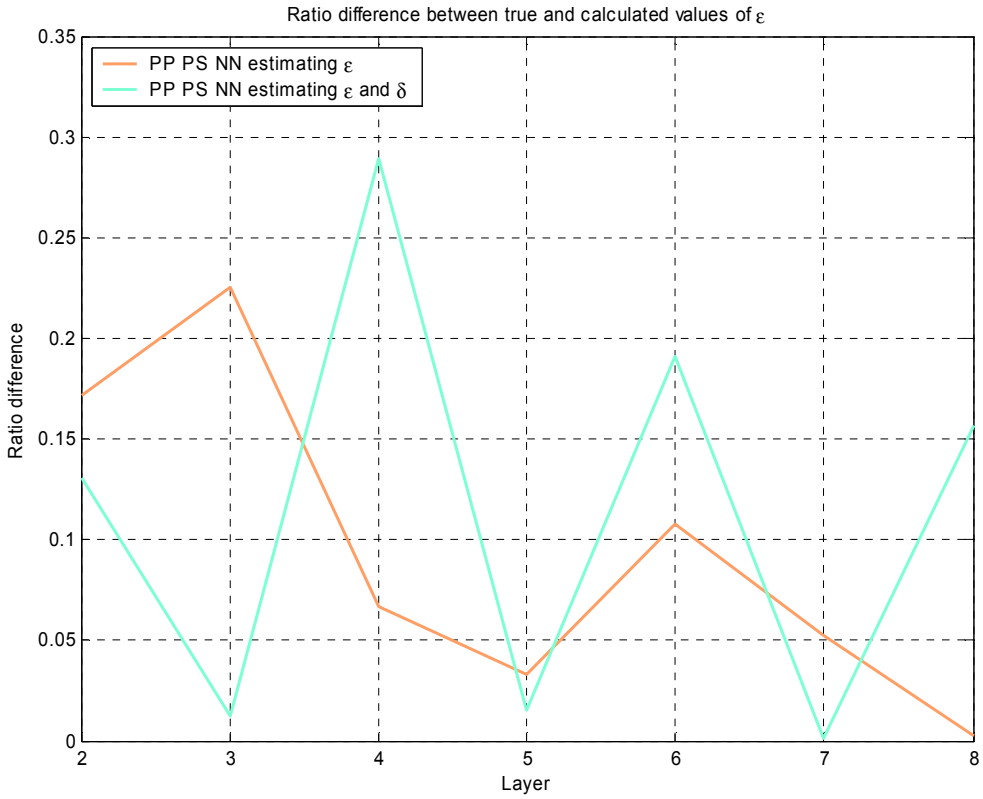

Figure 3-17 Ratio difference of calculated and true ε values calculated from joint PP and PS-wave inversion methods.

Table 3-13 True and calculated ε values from joint PP and PS-wave inversion methods

Layer	True ε	PP PS NN Estimating ε	PP PS NN Estimating ε and δ
1	0	0.007	0.00
2	0.05	0.041	0.057
3	0.1	0.077	0.101
4	0.15	0.140	0.107
5	0.2	0.193	0.203
6	0.25	0.223	0.298
7	0.3	0.284	0.300
8	0.2	0.201	0.169

Table 3-14 RMS errors for joint PP and PS-wave inversion methods used to estimate ε

Method	PP PS NN Estimating ε	PP PS NN Estimating ε and δ
RMS	0.0148	0.0255

The best estimation of ε is found from a neural network that estimates ε.

3.2.7 Comparison of methods

A summary of the RMS errors associated with each inversion method is provided in Figure 3-18 and Figure 3-19. Figure 3-18 displays the RMS error for δ estimation; while Figure 3-19 displays the RMS error for ε estimation. The y-axis has been plotted on a log scale.

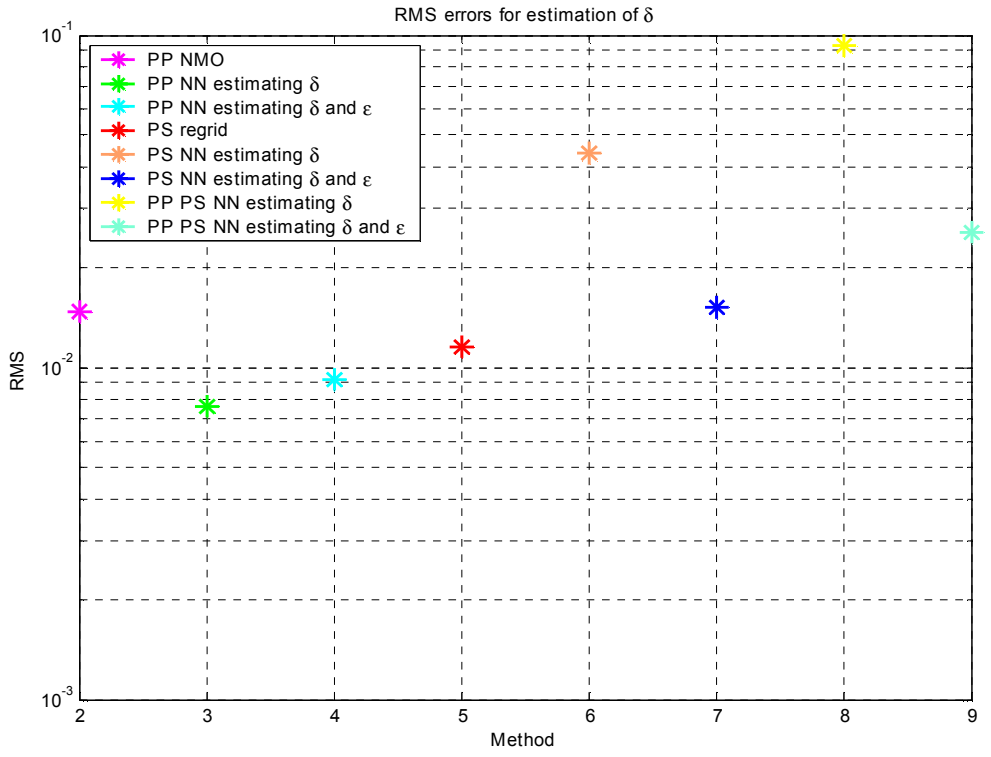

Figure 3-18 RMS errors for the estimation of δ. P-wave neural networks outperform other methods. The PS and PP-PS neural networks give the worst results.

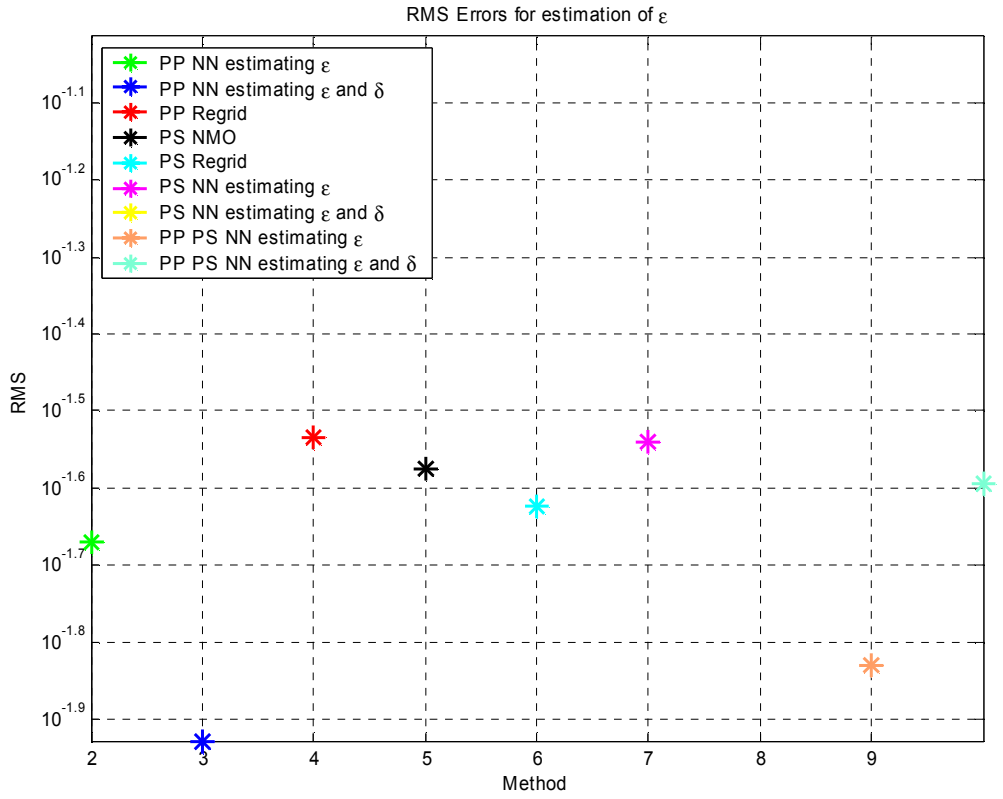

Figure 3-19 RMS errors for the estimation of ε. P-wave neural networks that estimate both parameters outperform other methods. The PS method gives the worst results

Figure 3-18 indicates that δ is best resolved from P-wave neural networks that invert for δ and Figure 3-19 indicates that ε is best resolved from P-wave neural networks that invert for both ε and δ.

3.3 Conclusion

Techniques discussed in chapter 2 to estimate the anisotropy parameters have been applied to a synthetic data set generated from an anisotropic model. P-wave neural network inversion techniques are the most robust method for estimating δ and ε.

Methods were assessed by comparing the RMS errors of each method. Overall, neural networks applied to compressional wave data gave the best results. Other methods

were very close in their performance, but overall it was the P-wave neural networks that proved to be most promising. The method determined to best recover δ was a neural network applied to P-wave data that estimates δ. It was able to delimit δ to within 5% of the true value. Conversely the method deemed to best determine ε was a neural networks applied to P-wave data that recovered both δ and ε. It was able to delimit ε to within 16% of the true value. When considering only converted wave data the PS regridding inversion gave the best results for both ε and δ. When considering compressional and converted wave data used in conjunction neural networks designed to recover both parameters gave the best results for δ and when designed to recover only ε gave the best results for ε.

Chapter 4 Field Data

Inversion methods determined to give optimal results for the synthetic data are applied to the Blackfoot study for estimation of ε and δ. Accordingly neural networks are applied to compressional wave data for the recovery of the anisotropic parameters.

4.1 Field Data

A 3.0 km 3C-2D seismic line was collected over the Blackfoot field in November of 1997. Blackfoot is located in Township 23, Range 23 west of the fourth meridian and is about 10-15 km southeast of Starthmore Alberta as seen in Figure 4-1.

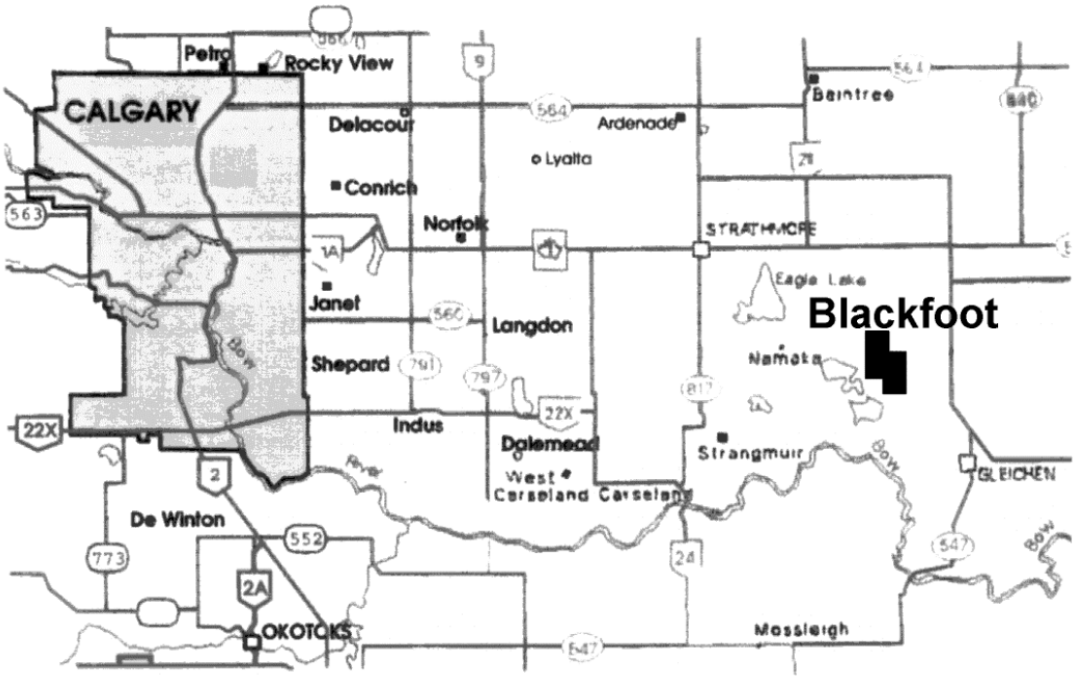

Figure 4-1 Map showing the location of the Blackfoot field in relation to the city of Calgary (Stewart et al., 1997).

4.2 Geology

The targets of the Blackfoot survey are Glauconitic incised valleys in the lower Manville Group of the Lower Cretaceous (Figure 4-2). The targets are lucrative with an average porosity of 18% and a cumulative production that exceeds 200 MMbbls oil and 400 BCF gas (Miller at al., 1995). The Glauconitic sandstones vary from 0-35 m in thickness and are located at a depth of roughly 1550 m in the area of study. The sand is very fine to medium grained in the eastern part of Alberta. (Miller at al., 1995).

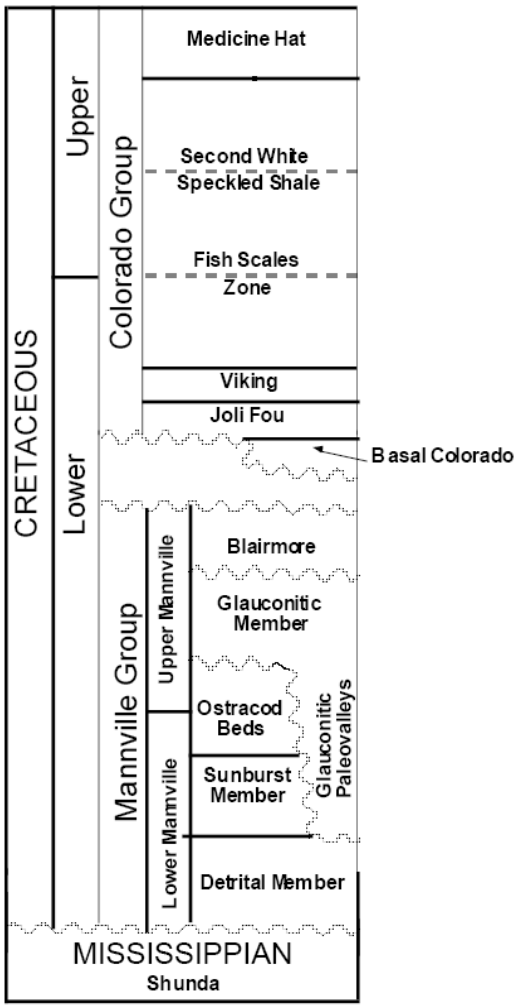

Figure 4-2 Stratigraphic sequence of the area of interest (Miller et al., 1995).

4.3 Evidence of anisotropy at Blackfoot

A test for anisotropy in the Blackfoot dataset was performed on the 1999 radial component by varying the values of the effective V_p/V_s ratio. No obvious anisotropic effects were observed; this is normal when analyzing a flat data set. However the most sound image of the channel was found using V_p/V_s =0.9. Thus, there is anisotropy in the area but it is weak (Lu and Margrave, 2001). Similar results were found by Cary and Lu (1999) who learned from a similar analysis that a great deal of resolution is lost when the effects of layered anisotropy are ignored. Hasse (1998) also explained non-hyperbolic moveout through anisotropy after discounting other potential explanations. Estimates of the anisotropic parameters are given by Elapavuluri (2003). Elapavuluri estimated δ from equation 2.51a and ε from a Monte Carlo inversion.

4.4 Seismic Survey

The survey involved the collection of a 3 km 3C-3D reflection profile. The shot interval was 20 m on the half station, the receiver interval was also 20 m except in the central 1 km where the spacing was 2 m. This thesis does not consider the high resolution data. 151 shots consisting of 4 kg charges were employed. The charges were loaded in holes at a depth of 18 m. Receivers were buried at a depth of 0.5 m to eliminate wind noise (Stewart et al., 1997).

4.5 VSP Survey

In 1995 a VSP survey was acquired in the PCP 12-16-23-23W4 well. The VSP survey was designed to record shots from a 3C-3D surface survey. A five level tool read 431 shots that consisted of 4 kg of dynamite buried in 18 m holes. Longer vertical arrays

were simulated by moving the receiver up and down hole for various shots, depth coverage was from 400 - 910 m (Zhang et al., 1996). Data was recorded for 4 s at 1ms intervals. Vertical P- and S-wave velocities were taken from this survey.

4.6 Outline of the method

A line named '20m vertical' was processed in Promax to obtain RMS velocities. The basic processing flow was

1) Geometry
2) AGC
3) Band-pass filtering
4) Sorting into CSP gathers
5) Velocity analysis

The RMS velocities were converted to interval velocities. Vertical compressional and shear velocities were found from the VSP data. Data was read into the neural networks that were developed during synthetic data simulation. The P-wave neural network that estimates δ was used to recover δ and the P-wave neural network that estimates both δ and ε was used to recover ε.

4.7 Estimation of ε and δ

The optimal inversion methods are applied to the Blackfoot data to recover ε and δ. Following Elapavuluri (2003) anisotropy parameters will be estimated in the formations listed in Table 4-2. Acronyms used to describe these formations are also listed in Table 4-2.

Table 4-1 Formation naming convention

Acronym	Formation Name
BFS	Base of Fish Scales
MANN	Blairmore-Upper Mannville
COAL	Coal Layer
GLCTOP	Glauconitic Channel
MISS	Shunda Mississippian

Inversions results are listed in Table 4-2 and

Table 4-3, for reference results from Elapavuluri (2003) are also shown. The results are also shown graphically in Figure 4-3 and Figure 4-4.

Table 4-2 Calculated δ values from Blackfoot P-wave neural networks and Elapavuluri (2003)

Formation	δ (estimated)	δ (Elapavuluri)
BFS	0.269	0.230
MANN	-0.005	0.040
COAL	0.284	0.240
GLCTOP	0.057	0.060
MISS	-0.121	0.000

Table 4-3 Calculated ε values from Blackfoot P-wave neural networks and Elapavuluri (2003)

Formation	ε (estimated)	ε (Elapavuluri)
BFS	0.232	0.060
MANN	-0.020	0.008
COAL	0.192	0.120
GLCTOP	0.030	0.006
MISS	0.010	0.001

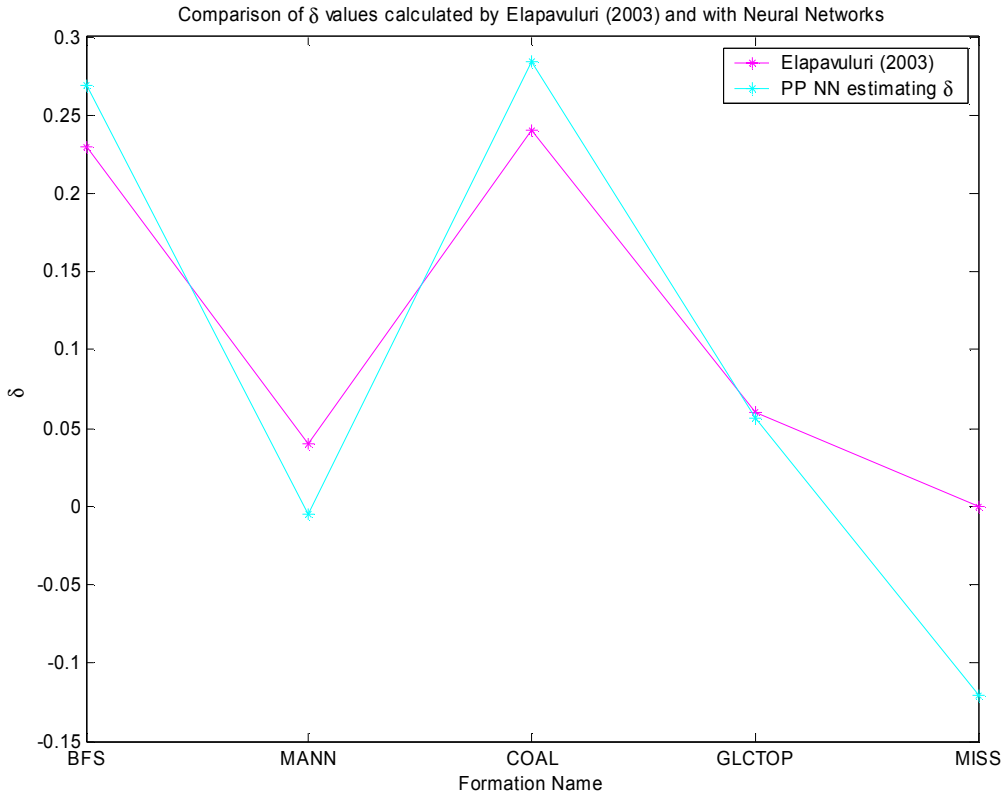

Figure 4-3 Comparison of δ recovered from P-wave neural networks that estimate delta and the results of Elapavuluri (2003) obtained from a Monte Carlo inversion.

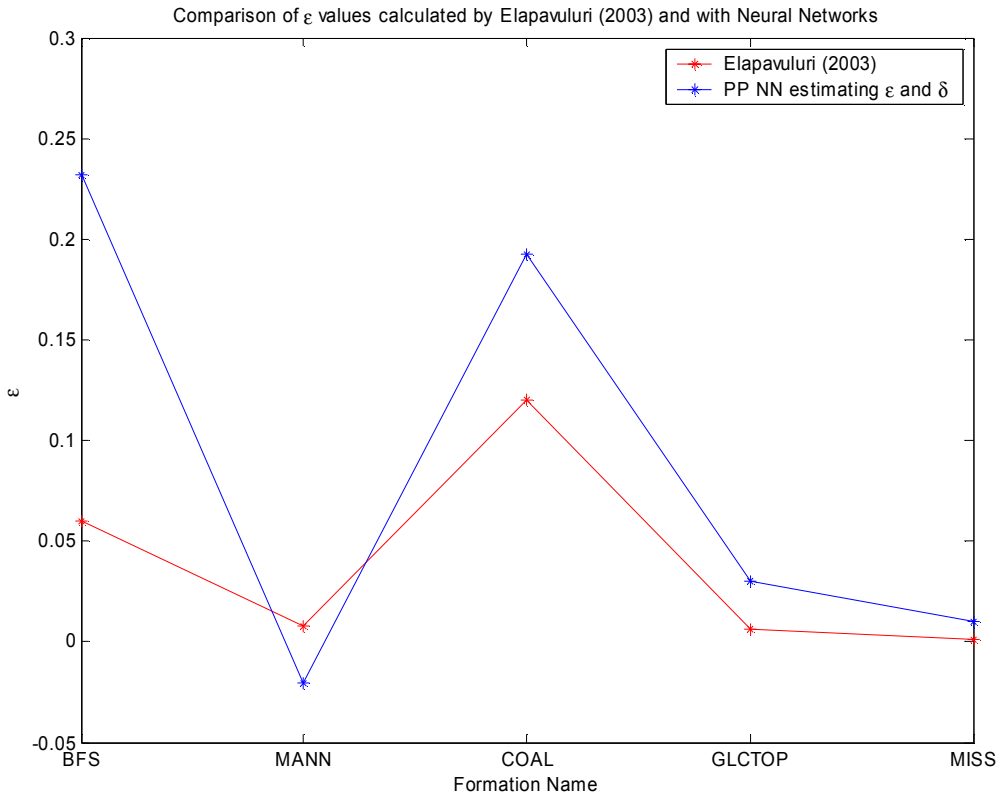

Figure 4-4 Comparison of ε recovered from P-wave neural networks that estimate both ε and δ and the results of Elapavuluri (2003) obtained from a Monte Carlo inversion.

Attempts to quantify anisotropy in the Blackfoot field are limited. Comparing with the results of Elapavuluri (2003) a fairly good match is obtained. The worst correlation is found at the MISS for δ and at the BFS for ε. The results are consistent with Thomsen (1986) where the sands show little anisotropy and the coals and shales display stronger anisotropy.

4.8 Conclusions and Discussion

Inversion methods found to be optimal from synthetic modelling were applied to the Blackfoot data set in order to recover ε and δ. The method of choice for recovering δ

was neural networks that estimate δ from P-wave data and for recovering ε was neural networks that estimate both ε and δ from P-wave data. The data was sorted into CSP gathers to perform the velocity analysis. Elapavuluri (2003) found that CSP gathers gave superior results when compared to CMP methods. Vertical velocities were obtained from a VSP survey. Results are consistent with Elapavuluri (2003) and Thomsen (1986), the coals and shales display a higher degree of anisotropy than the sands.

Chapter 5 Conclusion and Discussion

The earth is known to be anisotropic yet many processing algorithms assume isotropy. The most commonly encountered type of anisotropy is VTI. This thesis aims to determine if the anisotropic parameters (ε and δ) that describe P- and PS-waves can be best determined from compressional wave data, converted wave data or using both simultaneously and to determine which method best estimates these parameters. Methods were evaluated using the RMS error.

Anisotropic ray tracing was performed on a synthetic model consisting of 8 horizontal layers, each with its own unique physical properties, using NORSAR2D's anisotropic ray mapper. Results were convolved with a Ricker wavelet to create synthetic seismograms. Common scatter point gathers were formed in PROMAX and velocity analysis carried out. CSP gathers were chosen as they can be formed with slight dependence on velocity but still provide accurate velocities (Bancroft, 2004). This was also proven by Elapavuluri (2003). CSP gathers can and usually do have a higher fold than traditional CMP gathers as this is limited by the migration aperture and not the source receiver offset leading to higher resolution in the semblance analysis.

Several methods for the estimation of Thomsen's anisotropy parameters were proposed and investigated:

1. P-wave NMO equations
2. PS-wave NMO equations
3. P-wave regridding inversion
4. PS-wave regridding inversion
5. Neural networks applied to P-wave data estimating δ

6. Neural networks applied to P-wave data estimating ε
7. Neural networks applied to P-wave data estimating δ and ε
8. Neural networks applied to PS-wave data estimating δ
9. Neural networks applied to PS-wave data estimating ε
10. Neural networks applied to PS-wave data estimating δ and ε
11. Neural networks applied to PP- and PS-wave data estimating δ
12. Neural networks applied to PP- and PS-wave data estimating ε
13. Neural networks applied to PP- and PS-wave data estimating δ and ε

Methods were assessed by comparing the RMS errors of each method. Overall, neural networks applied to compressional wave data gave the best results. Other methods were very close in their performance, but it was the P-wave neural networks that proved to be most promising. The method determined to best recover δ was a neural network applied to P-wave data solving for δ. It was able to delimit δ to within 5% of the true value. Conversely the method that best determined ε was a neural network applied to P-wave data that recovered both δ and ε. It was able to delimit ε to within 16% of the true value. When considering only converted wave data the PS regridding inversion gave the best result for both ε and δ. When considering compressional and converted wave data used in conjunction neural networks designed to recover both parameters gave the best results for δ and when designed to recover only ε gave the best results for ε.

Having had success with synthetic data the algorithms that best defined the anisotropy parameters were applied to the Blackfoot data set. Evidence of anisotropy in the area had been shown. Inversion results were consistent with Elapavuluri (2003) who had previously used P-wave NMO equations to determine δ and a Monte Carlo inversion

to determine ε. Results are also in agreement with laboratory results of Thomsen (1986) where the coals and shales displayed a higher degree of anisotropy than the sands.

In conclusion a simple and robust algorithm is proposed for the estimation of Thomsen's anisotropy parameters, ε and δ. A neural network that estimates δ, has 29 neurons, uses vertical compressional and shear wave velocities and compressional interval velocity information for training and incorporates a tan sigmoid and linear transfer function will give optimal results for the estimation of δ. Similarly a neural network that estimates ε and δ, has 88 neurons, use vertical compressional and shear wave velocities and compressional interval velocity information for training and incorporates a tan sigmoid and linear transfer function will give optimal results for the estimation of ε.

List of References

Aki, K. and Richards, P.G., 2002, Quantitative Seismology second edition: University Science Books, Saulsalito, California.

Alkhalifah, T. and Tsvankin, I., 1995, Velocity analysis for transversely isotropic media: Geophysics, 60, 1550-1566.

Backus, G.E., 1962, Long-wave elastic anisotropy produced by horizontal layering: J. Geophys. Res., 70 3429.

Bancroft, J. C. and Wang, S., 2000, Processing converted-wave data using equivalent offset migration (EOM): 2000 SEG-EAGE Research Workshop.

Bancroft, J. C., 2004, A practical understanding of pre– and poststack migrations 6th edition, Geophysics 659 Course notes.

Berryman, J. G., 1979, Long-wave elastic anisotropy in transversely isotropic media: Geophysics, 44, 896-917.

Bolshix, C.F., 1956, Approximate model for the reflected wave traveltime curve in multilayered media: Applied Geophysics, 15, 3-14 (Russian).

Brittan, J., Warner, M., and Pratt, G., 1995, Anisotropic parameters of layered media in terms of composite elastic properties: Geophysics, 60, 1243-1248.

Byun, B., 1984, Seismic Parameters for Transversely Isotropic Media: Geophysics, 49, 1908-1914.

Cary, P. W. and Lu, H., 1999, Layered anisotropic CCP stacking of the Blackfoot 3C, 3D survey: CREWES Research Report, 11.

Castle, R.J., 1994, Theory of normal moveout: Geophysics, 59, 93-999.

Cerveny, V., 1972, seismic rays and ray intensities in inhomogeneous anisotropic media: Geophys. J. R. Astr. Sic., 29, 1-13.

Claerbout, J.F. and Black, J.L., 2001, Basic Earth Imaging, http://sepwww.stanford.edu/sep/prof/bei12.01.pdf.

Crampin, S., 1981, A review of wave motion on anisotropic and cracked elastic media: Wave Motion, 3, 343-391.

Crampin, S., Chesnokov, E.M. and Hipkin, R.G., 1984, Seismic anisotropy – the state of the art: II, Geophysical Journal of the Royal Astronomical Society, 76, 1-16.

Dayley, P.F. and Lines, L.R., 2004, Linearized quantities in transversely isotropic media: Can. J. Earth Sci., 41, 349-354.

Dayley, P.F. and Hron, F., 1977, Reflection and transmission coefficients for transversely isotropic media: Bull., Seis. Soc. Am., 69, 661-675.

Dayley, P.F. and Hron, F., 1979, Reflection and transmission coefficients for seismic waves in ellipsoidally anisotropic media: Geophysics, 44, 27-37.

Dix, C.H., 1955, Seismic velocities from surface measurements: Geophysics, 20, 68-86.

Elapavuluri, P. K., 2003, Estimation of Thomsen's anisotropic parameters from geophysical measurements using equivalent offset gathers and the shifted-hyperbola NMO equation, MSc Thesis University of Calgary.

Freeman, J. A. and Skapura, D. M., 1991, Neural Networks Algorithms, Applications and Programming Techniques: Addison-Wesley, Massachusetts.

Granli, J. R. Arnsten, B. Sollid, A. and Hilde, E., 1999, Imaging through gas-filled sediments using marine shear wave data: Geophysics, 64, 668-667.

Grechka, V. and Tsvankin, I., 1998a, Feasibility of nonhyperbolic moveout inversion in transversely isotropic media: Geophysics, 63, 957-969.

Grechka, V. and Tsvankin, I., 1998b, 3-D description of normal moveout in anisotropic inhomogeneous media: Geophysics, 63, 1079-1092.

Grechka, V. and Tsvankin, I., 1999, NMO surfaces and Dix-type formulae in heterogeneous anisotropic media, 69th Ann. Internat. Mtg: Soc. Of Expl. Geophys., 1612-1615.

Grechka, V., 2001, Seismic anisotropy: yesterday, today and tomorrow: CSEG Recorder, September, 2001, 9-10.

Hasse, A., Nov. 1998, Non-hyperbolic moveout in plains data and the anisotropy question: CSEG Recorder, 20-34.

Haykin, S., 1999, Neural networks a comprehensive foundation: Prentice-Hall Inc., New Jersey.

Helbig, K., 1964, Refraction seismics with an anisotropic overburden a graphical method of interpretation: Geophys, Prosp,. Eur, Assn, Geosci. Eng., 12 383-396.

Higham, J, D. and Higham, N. J., 2000, MATLAB Guide 2nd edition: Soc for Industrial & Applied Math, Philadelphia, PA.

Hornby, B., Johnson, C., Cook, J. and Coyner K., 1994, Ultrasonic laboratory measurements of the elastic properties of shales: 64th Annual Society of Exploration Geophysicists International Meeting, Los Angeles, California, October 23-28, - Expanded Technical Program Abstracts, Paper SL3 1, 1117-1120.

Isaac, J.H. and Lawton, L.C., 2004, A practical method for estimating effective parameters of anisotropy from reflection seismic data: Geophysics, 69, 681-689.

Jolly, R.N., 1956, Investigation of Shear Waves: Geophysics, 21, 9050-938.

Kendall, R. R., Gray, S. and Miao X., 2000, Anisotropic processing of converted wave data: Mahogany Field, Gulf of Mexico. SEG/EAGE Summer Research Workshop, Oct. 2000, Boise, USA.

Krebes, E. S., 2003, Seismic theory and methods: Course notes.

Love, A. E. H., 1927, A treatise on the mathematical theory of elasticity: Dover Publications, Inc,. N.Y.

Lu, H. and Margrave, G., 2001, Reprocessing the 1999 Blackfoot 3C-3D seismic data and anisotropy analysis for the radial component: CREWES Research Report, 13, 509-517.

Malovichko, A. A., 1956, A new representation of the traveltime curve of reflected waves in horizontally layered media: Applied Geophysics, 91, 47-53 (Russian).

Malovichko, A. A., 1979, Determination of the zero offset effective velocity and the degree of velocity nonhomogeneity from a single reflected wave traveltime curve in the case of horizontally layered media: Applied Geophysics, 95, 35-44 (Russian).

Margrave, G. F., 2002, Methods of Seismic Processing, Geophysics 557 Course notes.

Miller, S. L., Ayedemir, E. and Margrave, G., 1995, Preliminary interpretation of P-P and P-S seismic data from the Blackfoot broad-band survey: CREWES Research Report 1995.

Musgrave, M. J. P., 1970, Crystal Acoustics: Holden Day, San Francisco.

NORSAR 2D Ray Modelling user guide version 5.0 http://www.norsar.com/Seismod/Support/DocN2D.html.

Postma, G.W., 1955, Wave propagation in a stratified medium: Geophysics, 20, 780-806.

Sayers, C. M., 1999, Anisotropic velocity analysis using mode converted shear waves: Journal of Seismic Exploration, 8, 1-14.

Shearer, P. M., 1999, Introduction to Seismology: Cambridge University Press, United Kingdom.

Sheriff, R. E., 2002, Encyclopaedia Dictionary of Exploration Geophysics: Soc. Of Expl. Geophys., 2245-2248.

Stewart, R. R., Hoffe, B., Bland, H. C., Margrave, G., Gallant, E. V. and Bertram, M. B., 1997, The Blackfoot high-resolution 3-C seismic survey: design and initial results: CREWES Research Report 1997.

Taner, M. T., and Koehler, F., 1969, Velocity spectra-digital computer derivation and applications of velocity functions: Geophysics, 34, 859-881.

Tessmer, G., and Behle, A. F., 1988, Common reflection point data stacking technique for converted waves: Geophys. Prosp., 36, 671-688.

Thomsen, L., 1986, Weak Elastic Anisotropy: Geophysics, 51, 1954-1966.

Thomsen, L., 1999, Converted-wave reflection seismology over inhomogeneous, anisotropic media: Geophysics, 64, 678-690.

Tsvankin, I. and Grechka, V., 2001, Parameter estimation for VTI media using PP and PS reflection data, 71st Ann. Internat. Mtg: Soc. of Expl. Geophys., 857-860.

Tsvankin, I. and Thomsen, L., 1994, Nonhyperbolic reflection moveout in anisotropic media: Geophysics, 59, 1290-1304.

Tsvankin, I., 1995, Normal moveout from dipping reflectors in anisotropic media: Geophysics, 60, 268-284.

Tsvankin, I., 1996, P-wave signatures and notation for transversely isotropic media: Geophysics, 61, 467-483.

Van der Baan, M., and Kendall, J. M., 2002, Estimating anisotropy parameters and traveltimes in the τ-p domain: Geophysics, 67, 1076-1086.

White, J.E. and Sengbush, R.L., 1953, Velocity measurements in near-surface formations: Geophysics, 18, 54-69.

Winterstein, D.F., 1990, Velocity anisotropy terminology for geophysics: Geophysics, 55, 1070-1088.

Yilmaz, O., 1987, Seismic data analysis: processing, inversion, and interpretation of seismic data: Society of Exploration Geophysicists, Oklahoma.

Yilmaz, O., 2001, Seismic Data Processing: Society of Exploration Geophysicists, Oklahoma.

Zhang, Q., Stewart, R. R., Parkin, J. M., Sun, Z., 1996, Analysis of the 3C-3D VSP survey, CREWES Research Report, 8, 40-1 - 40-26.

Appendix 1 Velocities

Instantaneous velocity is defined as $V_{ins} = dz/dt$ and represents the actual velocity at a point in the subsurface at a specific location. To relate a specific depth with a specific time the average velocity is used

$$V_{ave}(t) = \frac{1}{t_2 - t_1}\int_{t_1}^{t_2} V_{ins}(t)dt\,. \tag{A1.1}$$

This is the velocity used for time to depth conversion. The RMS velocity is an apparent velocity and is defined in Claerbout, 2001 as

$$V(t)_{RMS} = \sqrt{\frac{1}{t_{2\_}t_1}\int_{t_1}^{t_2} V_{ins}(t)^2\,dt}\,. \tag{A1.2}$$

If velocity varies with depth, the traveltimes from a scatter point are roughly hyperbolic in an isotropic medium. If we break the event into many short line segments each segment gives a different $V_{RMS}(t_i)$ and we then have the tiresome job of determining the best model. Instead we fit the observational data to the best fitting hyperbola using a different velocity hyperbola for each apex i.e. find $V_{stk}(t_0)$ (a stacking velocity) so this equation will best flatten the data in (t,x)-space

$$t^2 = t_0^2 + \frac{x^2}{V_{stk}(t_0)^2}, \tag{A1.3}$$

where t_0 is the vertical two way travel time. A common application involves attaining interval velocities from measured RMS velocities. In the ith layer the interval velocity is v_{int_i} and the two way travel time Δt_{0_i}. The RMS velocity of a reflection from the bottom

of the i[th] layer is V_{RMS_i}. Applying equation A1.2 we define velocities from reflections at the first, second and third layers as (Claerbout, 2001)

$$V_{RMS\_1}^2 = \frac{V_{ins\_1}^2 \Delta t_{0\_1}}{\Delta t_{0\_1}}, \tag{A1.4}$$

$$V_{RMS\_2}^2 = \frac{V_{ins\_1}^2 \Delta t_{0\_1} + V_{ins\_2}^2 \Delta t_{0\_2}}{\Delta t_{0\_1} + \Delta t_{0\_2}}, \tag{A1.5}$$

and

$$V_{R3}^2 = \frac{V_{ins\_1}^2 \Delta t_{0\_1} + V_{ins\_2}^2 \Delta t_{0\_2} + V_{ins\_3}^2 \Delta t_{0\_3}}{\Delta t_{0\_1} + \Delta t_{0\_2} + \Delta t_{0\_3}}. \tag{A1.6}$$

Algebraic manipulation of equations A1.5 and A1.6 leads to the squared interval velocity $V_{\text{int}\_3}^2$

$$V_{\text{int}\_3}^2 = \frac{(\Delta t_{0\_1} + \Delta t_{0\_2} + \Delta t_{\_03}) V_{RMS\_3}^2 - (\Delta t_{01} + \Delta t_{02}) V_{RMS\_2}^2}{\Delta t_{03}}, \tag{A1.7}$$

or more simply

$$V_{\text{int}}(n) = \left(\frac{V_{RMS}^2(n)\tau_n - V_{RMS}^2(n-1)\tau_{n-1}}{\tau_n - \tau_{n-1}} \right)^{1/2}, \tag{A1.8}$$

where τ is now the two way vertical travel time. Examination of equation A1.7 leads to the limitation that the RMS velocity for the third layer can not be much smaller that than the RMS velocity estimate for the second layer. This is a Dix type integration or Dix equation (Dix, 1955).

Appendix 2 Sensitivity analysis

A2.1 Regridding Inversion

To determine how sensitive the regridding inversion algorithms are to errors in the input parameters sensitivity analysis was performed on the P- and PS-wave regridding inversion algorithms for the determination ε. A five, ten, fifteen and twenty-five percent error was added to δ, the shift parameter and the interval velocity for the P-wave regridding inversion and to the δ and interval velocity for the PS-wave regridding inversion. All other parameters were held constant at their true values and the resultant ε calculated.

Figures A2.1, A2.2 and A2.3 show the resultant ε and ratio differences for the P-wave regridding algorithm, while Figures A2.4 and A2.5 show results for the PS-wave regridding inversion.

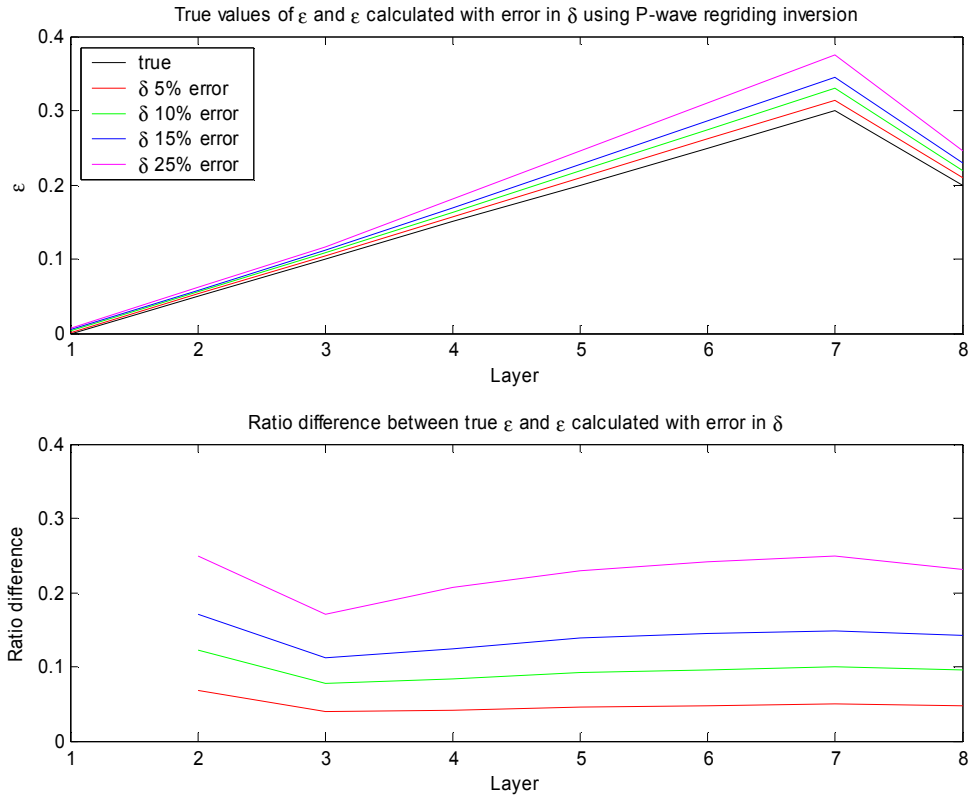

Figure A1-1Resultant ε values when error was added to δ. 5, 10, 15 and 25% error was added to the input δ value while all other parameters were held constant at their true values. It is seen that the deviation in the resultant ε is proportional to the error on the input value. The actual amount of error however is layer dependant

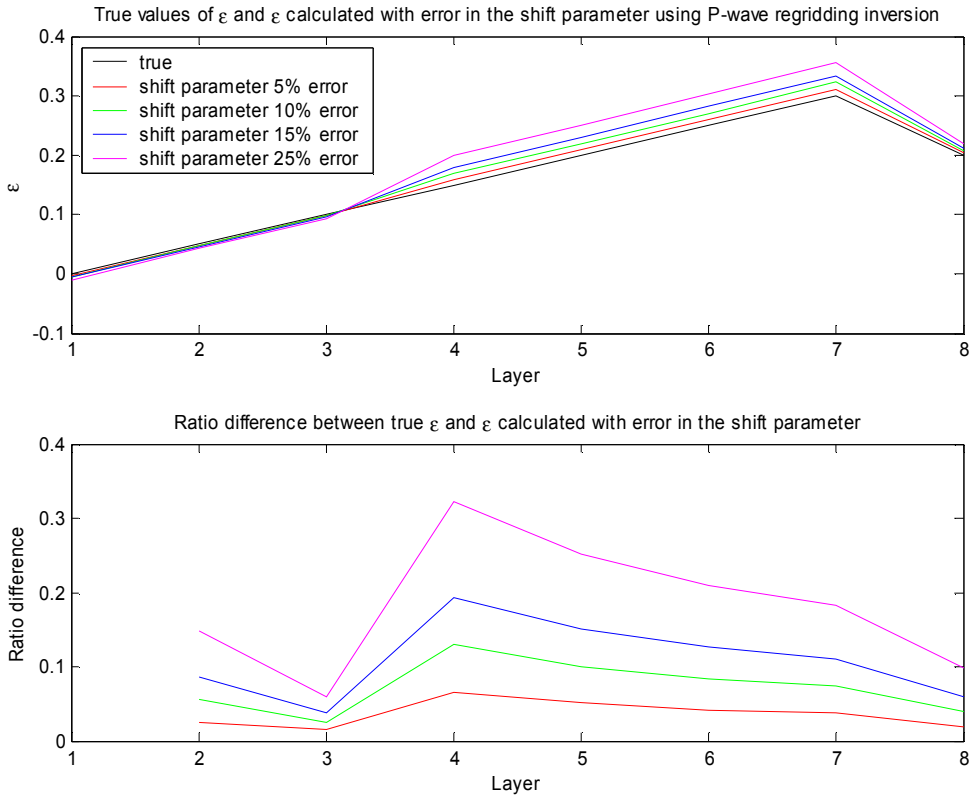

Figure A1-2 Resultant ε values when error was added to the shift parameter. 5, 10, 15 and 25% error was added to the input shift value while all other parameters were held constant at their true values. It is seen that the deviation in the resultant ε is proportional to the error on the input value. The actual amount of error however is layer dependant.

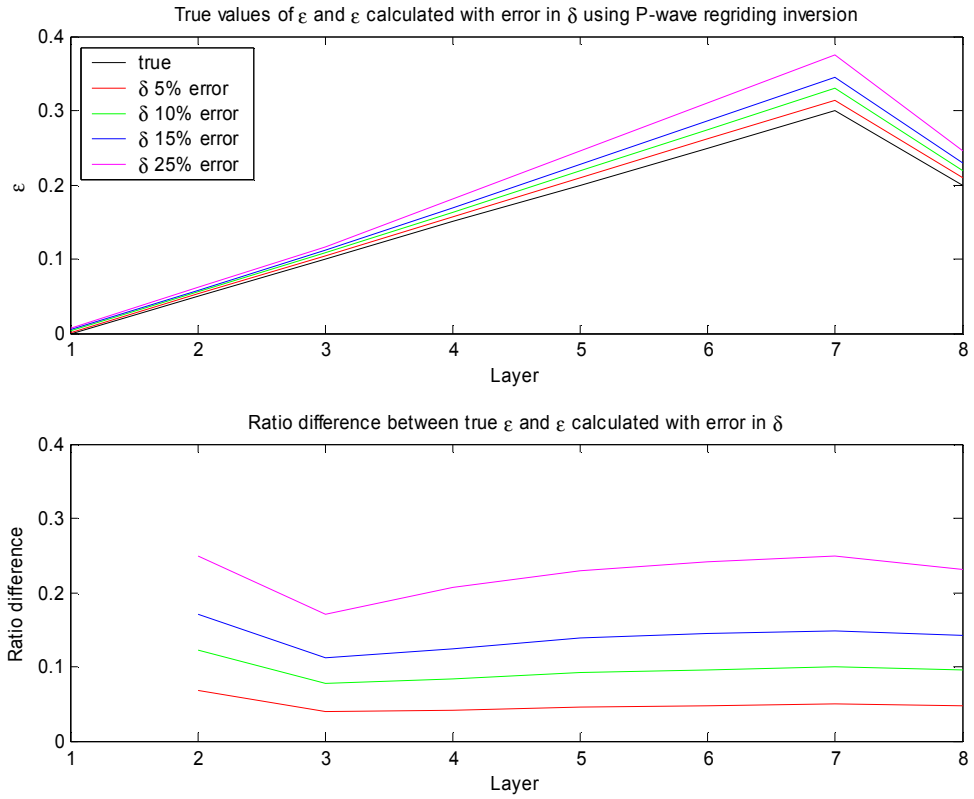

Figure A1-3 Resultant ε values when error was added to the velocity. 5, 10, 15 and 25% error was added to the input velocity value while all other parameters were held constant at their true values. It is seen that the deviation in the resultant ε is proportional to the error on the input value. The actual amount of error is layer dependant.

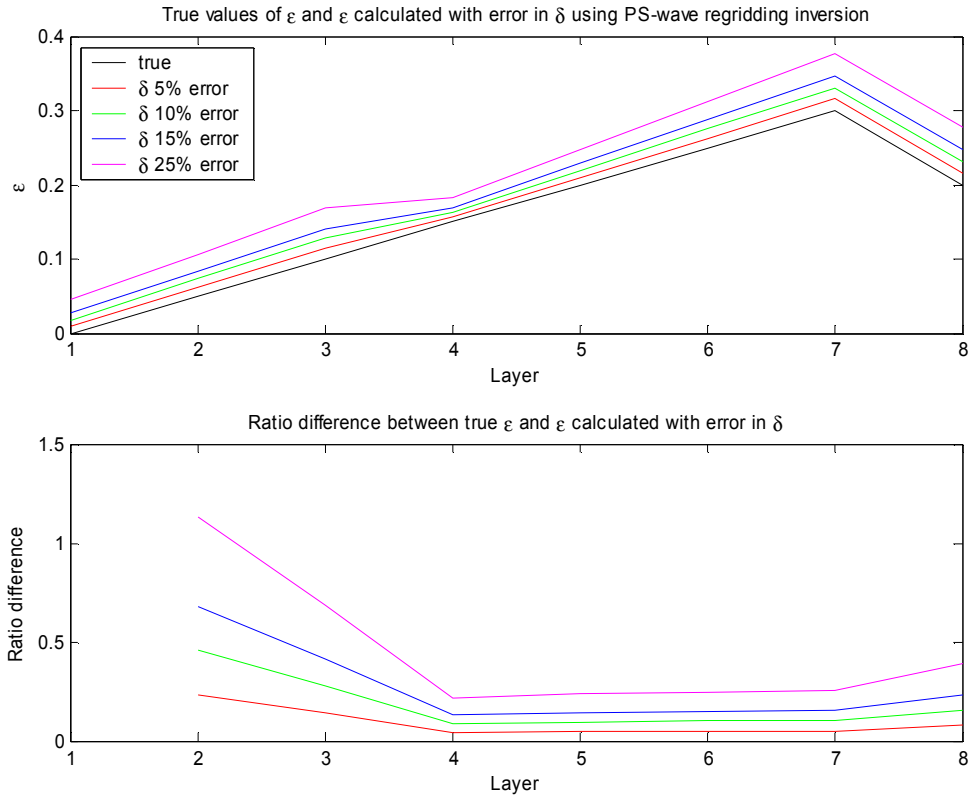

Figure A1-4 Resultant ε values when error was added to δ. 5, 10, 15 and 25% error was added to the input δ values while all other parameters were held constant at their true values. It is seen that the deviation in the resultant ε is proportional to the error on the input value. The actual amount of error is layer dependant.

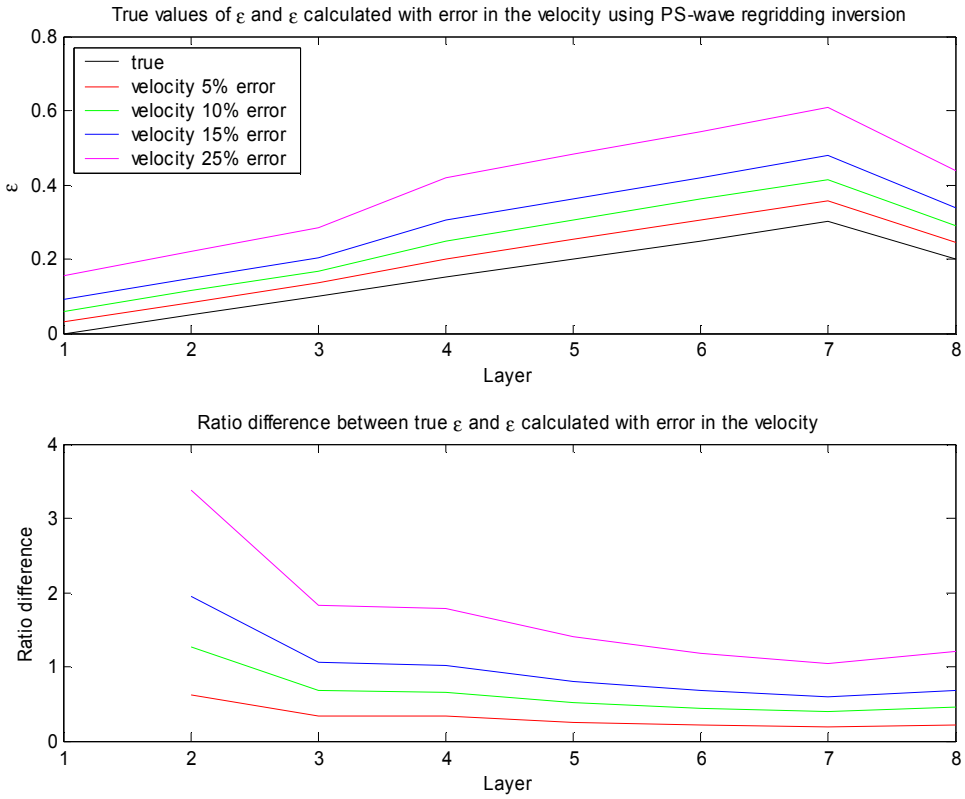

Figure A1-5 Resultant ε values when error was added to the interval velocity. 5, 10, 15 and 25% error was added to the input interval velocity values while all other parameters were held constant at their true values. It is seen that the deviation in the resultant ε is proportional to the error on the input value. The actual amount of error is layer dependant.

For P-wave regridding inversion errors in the calculated ε are linearly proportional to errors in δ and the shift parameter but not linearly proportional to errors in the velocity. Further P-wave regridding inversion is most sensitive to erroneous velocities. For PS-wave regridding inversion errors in the calculated ε are linearly proportional to errors in δ and the velocity. The PS-wave inversion algorithm is also most sensitive to errors in the velocity and is more sensitive to errors than is the P-wave regridding inversion. All results are layer dependent.

The RMS errors in the resultant ε values are tabulated in Table A1-1 and Table A1-2

Table A1-1 RMS errors in the calculated ε values from P-wave regridding inversion when the indicated amount of error is added to either δ, the shift parameter or the velocity

	5% error	10% error	15% error	25% error
δ	0.0087	0.0174	0.0261	0.0433
shift parameter	0.0075	0.0150	0.0224	0.0374
velocity	0.0234	0.0419	0.0566	0.0781

Table A1-2 RMS errors in the calculated ε values from PS-wave regridding inversion when the indicated amount of error is added to either δ or the velocity

	5% error	10% error	15% error	25% error
δ	0.0121	0.0242	0.0362	0.0602
velocity	0.0445	0.0912	0.1400	0.2441

These tables reinforce the notion that PS-wave regridding inversion is most sensitive to errors and that both algorithms are most sensitive to errors in the velocity

A2.2 Neural Network Inversion

To test the sensitivity of neural networks to erroneous velocities error was added to the input interval velocity in the P-wave inversion neural network that estimates δ and in the P-wave inversion neural network that estimates ε and δ. Results are displayed below in Figure A2.6 for δ estimation and in Figure A2.7 for ε estimation.

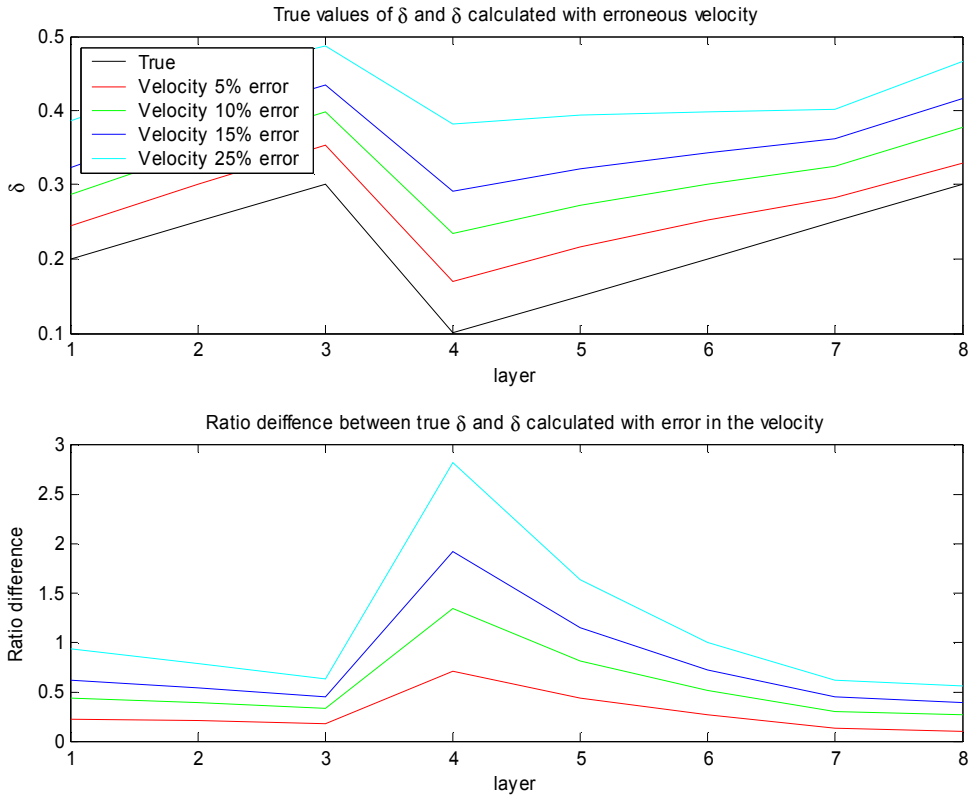

Figure A1-6 Resultant δ values when error was added to the velocity. 5, 10, 15 and 25% error was added to the input velocity value while all other parameters were held constant at their true values. It is seen that the deviation in the resultant δ is proportional to the error on the input value. The actual amount of error is layer dependant.

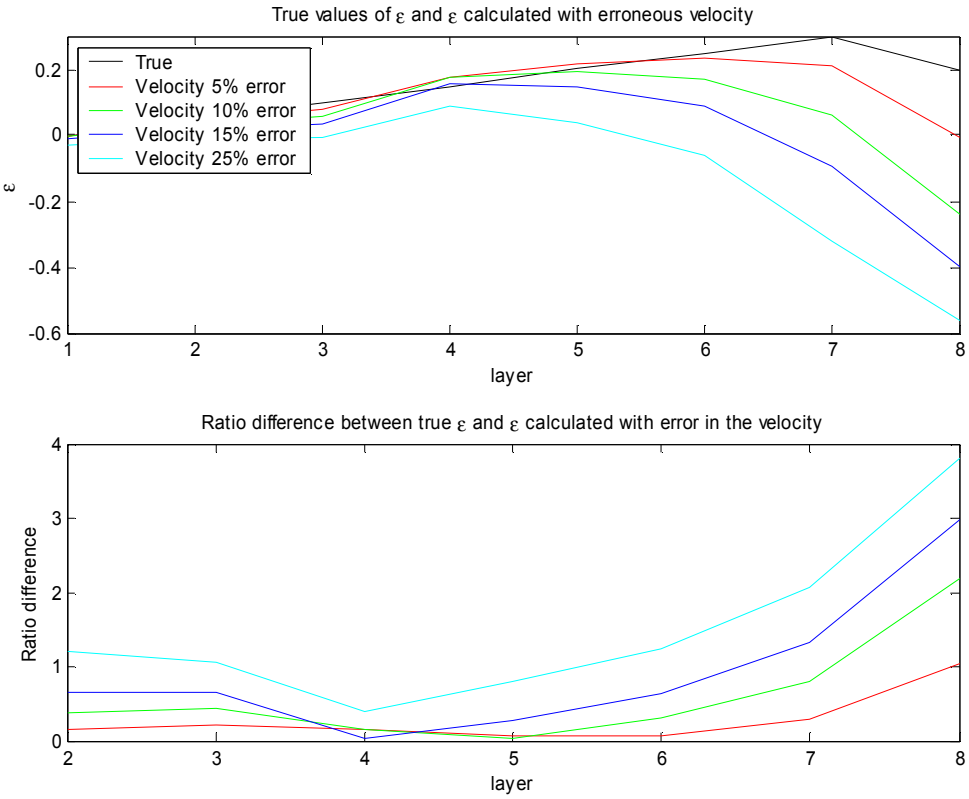

Figure A1-7 Resultant ε values when error was added to the interval velocity. 5, 10, 15 and 25% error was added to the input velocity values while all other parameters were held constant at their true values. It is seen that the deviation in the resultant ε is not proportional to the error on the input value and is layer dependant.

Results demonstrate that errors in the calculated δ are linearly proportional to the error in the interval velocity; the relation was not linear for the calculation of ε. Again the errors are layer dependant as in the case of regridding inversion. ε is more sensitive to errors in the input velocity than is δ.

RMS errors for the calculation of ε and δ when the velocity is in error are tabulated in Table A1-3 and Table A1-4

Table A1-3 RMS errors in the calculated δ values from P-wave neural networks when the indicated amount of error is added to the velocity

	5% error	10% error	15% error	25% error
velocity	0.06751	0.13548	0.19789	0.28977

Table A1-4 RMS errors in the calculated ε values from P-wave neural networks when the indicated amount of error is added to the velocity

	5% error	10% error	15% error	25% error
velocity	0.02298	0.065849	0.11041	0.15963

Examination of RMS errors indicates that δ is most susceptible to error when the velocity is erroneous.